Live-imaging reveals Coordinated Cell Migration and Cardiac Fate Determination during Mammalian Gastrulation.

Shayma Abukar[1,2], Peter A. Embacher[3], Alessandro Ciccarelli[4], Sunita Varsani-Brown[4], Jamie A. Dean[3], James Briscoe[4], Kenzo Ivanovitch[1,*]

[1]Developmental Biology of Birth Defects, Institute of Child Health, University College London, 30 Guilford Street, London WC1N 1EH, UK

[2]Institute of Cardiovascular Science, University College London, Gower Street, London WC1E 6BT, UK

[3]Department of Medical Physics and Biomedical Engineering, University College London, Gower St, London WC1E 6BT, UK

[4]The Francis Crick Institute, 1 Midland Road, London NW1 1AT, UK

[*] Corresponding author

E-mail: k.ivanovitch@ucl.ac.uk (K.I.)

Abstract

Heart development involves the specification of distinct sets of cardiac progenitors at various times and locations during ontogeny. Here, we used live imaging in mice from the initiation of gastrulation to heart tube formation stages to investigate the origin and migratory paths of cardiac progenitors. We tracked individual mesodermal cells, reconstructing the lineage tree of the cells and fates for up to four generations. Our findings revealed independent unipotent progenitors originating at specific times that exclusively contribute to the left ventricle/atrioventricular canal (LV/AVC) or atrial myocytes. LV/AVC progeny differentiated into myocytes early, forming the cardiac crescent, while atrial progenitors differentiated later and contributed to the venous poles of the heart tube during morphogenesis. We also identified short-lived bipotent and tripotent mesodermal progenitors that contribute to a diverse array of mesodermal cell types, illustrating early plasticity during gastrulation. Sister cells generated by multipotent progenitors dispersed more and adopted more diverse migratory trajectories within the anterior mesoderm space than those from unipotent progenitors. Together the data reveal the regulation of individual cell directionality and cardiac fate allocation within the seemingly unorganised migratory pattern of mesoderm cells.

Introduction

How cell fate specification and morphogenesis are coordinated in time and space to generate tissues and organs of unique forms and functions is central to developmental biology. This is evident during gastrulation when mesodermal cells acquire diverse cardiac fates and engage in complex cell movements to generate spatial patterns, such as a cohesive cardiac crescent, which transforms into a primitive heart tube.

Clonal analysis establishes lineage relationships between progenitors and their derivatives. In the gastrulating mouse embryo, tracking the derivatives of single progenitors led to the finding that progenitors are assigned to specific anatomical locations in the heart prior to the formation of the heart fields [1-4]. Unipotent *Mesp1*+ progenitors are solely destined for the left ventricle (LV) and atria myocardium can be distinguished from unipotent endocardium progenitors [2]. Additional clonal analysis of *Hand1*+ progenitors located at the embryonic/extraembryonic boundary in the early gastrulating embryo identified bipotent and tripotent progenitors. These progenitors generated LV/AVC myocytes in addition to pericardium, epicardium, and extraembryonic tissues [1].

One limitation of clonal analysis, however, is that the history of the cells is *deduced* by analysing descendants at the endpoint. It does not allow the identification of the progenitors' initial locations or subsequent migratory paths in the embryo. Single-cell tracking in live-imaging is needed for this and is the most rigorous approach to reconstituting cell lineages, identifying when cardiac progenitors become lineage-restricted during gastrulation and enabling migration analysis [5].

53 A recent live-imaging analysis uncovered the dynamics of mesodermal cell migration during
54 mouse gastrulation [6]. This analysis revealed that cells dispersed extensively in the embryo,
55 with clearly separate movements of daughter cells, suggesting cell identity may not be fixed
56 but instead influenced by the position of the cells at the end of the migration period.
57 However, as Dominguez et al. discussed, the motility of mesodermal cells is unlikely to be
58 completely random. There may be some regulation of directionality of individual cell
59 migration to ensure progeny migrate to their correct locations and establish spatial patterns,
60 including the cardiac crescent and distinct LV/AVC and atrial progenitor domains [7-9].
61 Indeed, a previous migration analysis showed mesodermal cell migrate with directionality
62 during mouse gastrulation [10]. Thus, early mammalian mesoderm migration may exhibit
63 some degree of determinism. This is reminiscent of an evolutionarily distinct species, the
64 ascidian, in which a small number of genealogically related and determined heart progenitors
65 migrate with predetermined directionally [11]. However, it is not known whether progenitors
66 adopt more stereotypical migratory trajectories, once committed to specific cardiac fates in
67 the context of mammalian gastrulation.

68 Here, through long-term live imaging and single-cell tracking in mice, spanning from the
69 initiation of gastrulation to the stages of heart tube formation, our goal was to reconstitute the
70 lineage tree of cells and assess how the migratory paths of cells relate to their eventual
71 cardiac fate within the seemingly unorganised migration pattern.

72 Results

73 Development and characterisation of *cTnnT-2a-eGFP* mice

74 To track cardiomyocytes in vivo, we developed a knock-in mouse reporter line *cTnnT-2a-*
75 *eGFP* where the *eGFP* sequence is inserted downstream of the endogenous *cardiac troponin*

76 *T* (*cTnnT*) loci. A virus-derived 2a self-cleaving peptide inserted between the *cTnnT* and
77 *eGFP* coding sequence ensures co-expression of both cTnnT and eGFP proteins (Fig.1 A)
78 [12]. The *cTnnT-2a-eGFP* line was maintained as homozygotes. Animals are viable and
79 indistinguishable from heterozygotes. Whole-mount immunostaining for cTnnT confirmed
80 specific eGFP expression in cTnnT+ cardiomyocytes at E8 -heart tube stage- and E12.5
81 (Fig.1 B-C).

82 We first analysed cardiac differentiation dynamics in real time using multiphoton live-
83 imaging and the cardiomyocyte *cTnnT-2a-eGPF* reporter line (Fig.1 D). We combined the
84 *cTnnT-2a-eGPF* reporter with the *Bre:H2BCerulean* BMP reporter [7], which expressed
85 cerulean in the lateral plate mesoderm. We found initial sparse GFP positive cells appearing
86 within the Bre-Cerulean positive lateral plate mesoderm at E7.5 - consistent with initial
87 sparse cTnnT protein distribution found in the lateral plate mesoderm [13]. This was followed
88 by the establishment of the cardiac crescent epithelium-like structure and primitive heart tube
89 (Fig.1 D). We conclude that the *cTnnT-2a-eGFP* reporter faithfully identifies cardiomyocytes
90 among a population of lateral plate mesodermal cell derivatives.

91 **Establishing long term light-sheet live microscopy for cardiac lineages analysis**

92 Using live-imaging and single-cell tracking in conjunction with the cardiomyocyte *cTnnT-2a-*
93 *eGPF* live-reporter, we set out to reconstitute the lineage trees of mesodermal cells and
94 identify the initial mesodermal progenitors that contribute solely to the heart tube in the
95 gastrulating mouse embryo (Fig.2 A). To achieve this required culturing and imaging early
96 mouse embryos from the onset of gastrulation to the heart tube stage (i.e. ~25-35 hours).

97 We found the Viventis LS1 open-top light-sheet microscope allowed the culture of early
98 mouse embryos over long periods of embryonic development (>24 hours). Incubation media

99 was stable and could be exchanged during acquisition. A large media volume (~1ml)
100 improved embryonic viability for long-term imaging. Embryos cultured from E6.5 and for 35
101 hours developed normally; a cardiac crescent formed and generated a heart tube
102 corresponding to E8 embryos.

103 To permanently label mesodermal cells and their progeny at a density suitable for live cell
104 tracking, we used an inducible $T^{2a\text{-}cre/ERT2}$ mouse combined with $R26^{tdomato}$ reporter and
105 administered intermediate doses of tamoxifen (0.002mg/bw) at stages encompassing E5 to
106 E6.5 [7]. We first administered tamoxifen earlier – (at E5) - and cultured embryos in
107 tamoxifen-free culture media, from before the start of the gastrulation period and onset of
108 T/Bra expression in the primitive streak and mesoderm – (at E6) -. In these conditions, no
109 tdTomato expressing cells could be identified in the intra-embryonic mesoderm over ~11
110 hours of live-imaging acquisition (Figure 2-supplementary figure 1 A). This confirms that
111 creERT2 activity in $T^{2a\text{-}cre/ERT2}$ embryos requires *T/Bra* expression [7]. In the absence of
112 tamoxifen, rare tdTomato-positive cells were identified in only one embryo (not shown),
113 confirming that tdTomato widespread mesodermal expression in $T^{2a\text{-}cre/ERT2}$ $R26^{tdTomato}$ embryos
114 requires tamoxifen.

115 We generated three light-sheet live-imaging datasets spanning 23 to 35 hours of mouse
116 embryonic development from gastrulation – (E6.5-E7) - to heart tube stage (Fig.2 B and
117 Videos 1-3). Embryos were imaged for 1 minute at 2 minutes intervals. Raw data amounts to
118 5-7 terabytes per experiment, representing up to half a million images. To correct for drift
119 during acquisition, BigSticher [14] was used to register the datasets in 4D as previously
120 described [6]. Movies were synchronised according to the timing of appearance of the cardiac
121 crescent and heart tube inflows (Figure 2-supplementary figure 2 A-K).

122 Each movie contains up to ~1000 time points, and a small percentage (<1%) of linkage
123 inaccuracy between cells could lead to lineage misinterpretation that propagates over the
124 course of the movie. Automated cell tracking methods have seen advancements [15, 16].
125 However, achieving the level of precision necessary to reconstitute cell lineages remains
126 challenging. To obtain accurate cell lineages, we manually tracked single cells by visualising
127 them at successive time points from the beginning to the end of the movie using Massive
128 Muti-view Tracker (MaMut) [5] (Videos 1-3). We interrupted a track when it was impossible
129 to identify the same cell across two successive time points unequivocally. A total of 61
130 mother cells were tracked for up to 4 generations.

131 We determined the identity of the final daughters based on their location in the heart tube.
132 The heart tube is formed by an inner endocardial layer ensuring the presence of a circulatory
133 system, a myocardial layer formed by cTnnT positive cardiomyocytes and derived from the
134 splanchnic mesoderm, and an outer layer derived from the somatic mesoderm called the
135 pericardium. We could discriminate these cell types in our live-imaging datasets (Videos 4-
136 6). Moreover, endocardial cells had distinct spindle-like shapes, displaying protrusions and
137 transmigrating across the myocardium (Fig. 4D and Video 6, n=4). Cardiomyocytes were
138 further distinguished by their higher levels of *cTnnT-2a-eGFP* reporter expression (Material
139 and Methods and Figure 2-supplementary figure 3 A-D). Finally, the locations of the
140 myocyte *cTnnT-2a-eGFP*+ cells within the heart tube indicated their fates. The heart tube has
141 an inverted Y shape, and the two arms of the Y -or inflows-, positioned inferiorly, are fated to
142 become the atria, with the stem of the Y becoming the left ventricle (LV) and atrioventricular
143 canal (AVC) [17]. In what follows, we describe the lineage trees and timing for mesodermal
144 progenitors' specification into distinct cardiac lineages.

145 **Distinct mesoderm contributes to the heart tube and inflows myocardium.**

146 We first addressed the timing of LV/AVC and atria myocyte lineage segregation. From our 3
147 datasets, we identified 29 progenitors contributing to at least one *cTnnT-2a-eGFP*+ myocyte
148 (Fig. 3A). We analysed their progenies' locations in the heart tube and found they established
149 a clonal boundary located at the junction between the LV/AVC and atria myocyte
150 compartments suggesting that atrial and LV/AVC progenitors have distinct mesodermal
151 origins (Fig.3 Bi-iii and Figure 3-supplementary Figure 1 Ai-vi). Among these 29
152 progenitors, 14 contributed to the LV/AVC and 13 to the atria. None contributed to clones
153 spanning the LV/AVC and atria compartments. Two additional progenitors generated *cTnnT-*
154 *2a-eGFP*+ cells in deeper z-locations within the heart tube (~ -250 μm).

155 The LV/AVC and atrial myocyte lineages have distinct temporal origins in the mesoderm.
156 Early mesoderm contributed to the LV/AVC, while late mesodermal cells generated atrial
157 myocytes. (Fig. 3Bi). This observation is in line with the previous hypothesis that atrial and
158 LV/AVC compartments have distinct spatial and temporal origins during gastrulation in the
159 mouse [7-9].

160 The LV/AVC progenitors are born first and differentiate into *cTnnT-2a-eGFP*+ myocytes
161 before other cardiomyocytes. This establishes the initial cardiac crescent within a ~10-hour
162 period with the first LV/AVC progeny differentiating at ~E6.5 + 15 hours and the last at
163 ~E6.5 + 25-27 hours. Atrial progenitors are born the latest, differentiate the latest - from
164 ~E6.5 + 25-27 hours -, and are recruited to posterior regions during the folding of the cardiac
165 crescent into the heart tube. This establishes the inflows (Fig.3 D-E and H-I). A subset of
166 mesoderm progenitors located in the inflow regions did not become *cTnnT-2a-eGFP*+ (n=6);
167 however, these cells may become positive at later stages.

168 Myocytes developed concurrently within each lineage (Fig.3 F). The time intervals between
169 the first and the last daughter to transition into cTnnT-2a-eGFP+ myocytes were 2 hours and

170 30 minutes on average for LV/AVC lineages, and 2 hours and 35 minutes on average, for
171 atrial lineages. Notably, the differentiation timing varied among lineages, with some
172 displaying greater synchrony than others. For instance, in 3 out of 29 lineages, the mother cell
173 generated LV/AVC cTnnT-2a-eGFP+ myocyte daughters in more than 5 hours. In contrast,
174 in 8 out of 26 lineages, all daughters transitioned into cTnnT-2a-eGFP+ myocytes in less than
175 one hour.

176 Together, the live-imaging analysis shows that the heart tube is established by at least two
177 sets of independent LV/AVC and atrial myocyte progenitors generated from early and late
178 mesoderm and differentiating into myocytes at different embryonic stages.

179 **Identification of unipotent, bipotent and tripotent cardiac progenitors.**

180 We next sought to address if mesodermal progenitors contributing to the LV/AVC myocytes
181 had the potential to generate additional mesodermal lineages. We identified unipotent
182 LV/AVC progenitors contributing only to *cTnnT-2a-eGFP*+ myocytes (n=9/14) (Fig.3 A, C
183 and H-H'). However, challenging the notion that mesodermal lineages are locked into
184 specific fates early [18], we found bipotent progenitors contributing to LV/AVC myocytes
185 and the endocardium (n=2/14) (Fig.3 A and Fig.4 C, C') as well as the LV/AVC myocytes
186 and extraembryonic mesoderm (n=1/14) [1]. We also found tripotent progenitors contributing
187 to LV/AVC myocytes, extra-embryonic mesoderm, and pericardium (n=1/14) and LV/AVC
188 myocytes, endocardium and extra-embryonic mesoderm (n=1/14) (Fig.3 A and Fig. 4 -
189 supplementary Figure 1 A, A').

190 LV/AVC myocyte progenitors were located in the proximal mesoderm, intermingled with
191 additional progenitors contributing to exclusively non-myocyte *cTnnT-2a-eGFP*- cardiac
192 lineages (n=8). We identified unipotent pericardial and endocardial progenitors (n=5/8)

193 (Fig.3 A and Fig.4 A, A') and bipotent progenitors generating endocardial and extra-
194 embryonic mesodermal cells (n=2/8) (Fig.3 A and Fig.4 B, B') and endocardial and
195 embryonic mesodermal cells (n=1/8) (Fig.3 A). An additional bipotent progenitor located in
196 proximity to an LV/AVC myocyte progenitor (cell-cell distance: 29 μm), generated highly
197 migratory endothelial-like daughter cells located in the embryonic mesoderm and extra-
198 embryonic mesoderm (Fig.3 A and Fig.4 E, E').

199 Bipotent progenitors contributing to cardiac and extra-embryonic mesodermal cells were
200 preferentially located at the extra embryonic/embryonic border (Fig.3 C). However, other
201 bipotent/tripotent progenitors were intermingled with unipotent LV/AVC progenitors within
202 the proximal mesoderm, with no clear spatial pattern identifiable. The initial cells' locations
203 in the early proximal mesoderm seems, therefore, not to correlate with specific mesodermal
204 fates. However, tracking a greater number of cells would be required to fully address this
205 question. In line with previous live-imaging analyses [6, 7], the distal mesoderm migrated to
206 more medial locations (Fig.3 C -dark red cells), known to provide progeny for the right
207 ventricle, outflow tract and branchiomeric muscles [19-22].

208 In the late mesoderm, we identified 6 unipotent atrial myocyte progenitors out of the 13
209 progenitors contributing to the *cTnnT-2a-eGFP*+ atria myocytes. Longer tracks
210 encompassing later stages are required to determine if the remaining progenitors contribute to
211 atria *cTnnT-2a-eGFP*+ myocytes entirely or also to additional lineages. Moreover, we found
212 additional progenitors contributing exclusively to *cTnnT-2a-eGFP*- daughters located in the
213 inflow's regions of the heart tube and posterior lateral plate mesoderm (n=16 lineages,
214 identified as meso GFP- in Fig.3 A). Additional markers or longer movies will be required to
215 determine the identity of these cells. A subset of these cells had spindle-like shapes and were
216 identified as endothelial-like cells (n=6, Fig.3 A).

217 Together, the live imaging analysis of lineages shows that the early mesodermal cells harbour
218 a previously underappreciated plasticity and diversity of fates during gastrulation [1]. Yet,
219 their ability to alternate fates seems to be rapidly reduced. 20 out of 35 initial mother cells
220 contributing to cardiac fates were unipotent, and in all cardiac lineage trees with two or three
221 fates (n=8), progeny become lineage-restricted early, during migration, before the onset of
222 *cTnnT-2a-eGFP*+ expression in the embryo (Fig.3 G). All 6 bipotent progenitors analysed
223 generated unipotent progenitors after the first cell division; and the two tripotent progenitors
224 generated unipotent daughters after the first and second cell division (Fig.3 A). These results
225 are consistent with previous clonal analyses suggesting that early mesodermal progenitors are
226 rapidly specified into discrete fates after the initiation of gastrulation [2-4].

227 **Migration analysis in lineages reveal hidden patterns of cell migration.**

228 Previous live analysis of cell trajectories during gastrulation revealed apparently chaotic
229 individual cell movements during migration [6]. Consistent with this analysis, we found that
230 mesodermal cells dispersed extensively during migration with strong separating movements
231 between daughter cells (Fig.5 A). We analysed distances between the first two daughters
232 (coordinates were taken 10 minutes after the first cell division - Timepoint 0 -, and last time
233 point before the daughters' subsequent cell division - Timepoint 1 -) and granddaughters
234 (final time point at which all granddaughter cells exist, we only considered branches lasting
235 at least 4 hours into the cell cycle to allow sufficient cell migration - Timepoint 2 -) in each
236 lineage. Distances between daughters and granddaughters gradually increased, reaching
237 considerable distances within a single lineage (up to 365 μm) (Fig.5 A). We noted, however,
238 that distances were highly heterogenous; a proportion of the progeny generated less
239 dispersive daughters with separating distances of less than 50 μm between them (11 out of 27
240 cardiac lineages).

241 One possibility for the observed heterogeneity in these distances is that the daughters
242 generated by unipotent progenitors exhibit less dispersive migratory paths than those
243 generated by bipotent progenitors (Fig.5 B). To test if this correlation was true, we analysed
244 cell movements in lineages, taking advantage of our lineage analysis from the live-imaging
245 data.

246 We first analysed if distances between daughters and granddaughters generated by bipotent
247 cardiac progenitors were greater than those generated by unipotent cardiac progenitors.
248 Immediately after the first cell division, we found no distance differences between sisters
249 generated from unipotent or bipotent progenitors. Distances between sisters with shared
250 cardiac fates became smaller on average compared to distances between sisters of distinct
251 cardiac fates (Fig.5 C). A similar difference was found when cell coordinates were sampled
252 before the onset of *cTnnT-2a-eGFP* expression (Fig.5 D-H). Thus, unipotent cardiac
253 progenitors generated less dispersed daughter and granddaughter cells than bipotent
254 progenitors. Distances between sisters could be high in non-cardiac lineages generating only
255 extra embryonic mesoderm, occasionally reaching distances of over 300 μm (Fig.5 G).

256 The observation that sister cells sharing the same fate end up in the same position in the
257 embryo may be due to these cells following the same migratory paths. Alternatively, pairs of
258 sister cells could independently follow distinct migratory trajectories and, by chance,
259 converge into similar embryonic territories. To address this question, we analysed if sisters
260 harbouring a shared cardiac fate migrated in closer proximity than sisters with divergent
261 fates. We used a dynamic time warping (DTW) algorithm (Fig.5 I and Material and Methods)
262 that accounts for instances where cells may exhibit similar behaviours but with temporal
263 shifts [23, 24]. We selected time periods such that sisters' trajectories started and ended at the

264 same time and calculated the cumulative distances between the two trajectories that yielded
265 the optimal alignment in each pair of sister cells (i.e. a DTW distance).

266 On average, unipotent progenitors generated sisters with lower DTW distances than bipotent
267 progenitors (Fig.5 J-L). We observed four case (out of 20) where a unipotent progeny
268 generated sisters with a distinct migratory trajectory (log DTW value > 8.5), and two cases
269 (out of 10) where bipotent progenitors produced sisters with similar migratory paths but
270 distinct fates (log DTW value < 8.5) (Fig.5 J). This suggests that sisters can occasionally
271 diverge in their migratory paths yet adopt a similar cardiac fate; or adopt similar paths and
272 contribute to different fates. (Fig.5 J-L and Figure 5 -supplementary 1 A-B). However, the
273 majority of sister pairs with the same cardiac fate exhibited notably similar migratory
274 trajectories (Fig .5 N-S). To rigorously assess this observation, we employed a permutation
275 test. We created 100.000 permutations by pooling all log DTW distances and randomly
276 assigning them to either unipotent or bipotent conditions. In each permutation, we computed
277 the difference in average log DTW values between sister cells with shared fates and those
278 with distinct fates. This iterative process generated a null distribution, allowing us to test
279 whether unipotent progenitors are producing sisters with more similar trajectories compared
280 to bipotent progeny (Fig.5 Supplementary Figure 1C). Our analysis revealed that this was the
281 case (p-value= 0.00027). Plotting the DTW values over time shows that the migratory
282 trajectories of sister cells sharing the same fates are similar throughout their entire migratory
283 periods and any observed similarity is not attributed to systematic smaller DTW-
284 contributions towards the end of the trajectory (Fig.5 M). Moreover, the DTW values
285 diverged early in sister cells with distinct fates, indicating that their migratory trajectories are
286 rapidly distinct at the beginning of their migration when the different fates head off towards
287 different destinations (Fig.5 M). The results suggest that pairs of sisters with shared fate
288 maintain closer proximity throughout their entire migration periods, exhibiting more

289 analogous migratory paths compared to sister cells that adopt distinct fates (Fig.5 M and N-
290 S).

291 Discussion

292 Our findings illustrate the progression of cardiac mesodermal lineages during gastrulation
293 (Fig.6). Using live-imaging and single cell tracking, we reconstructed cardiac mesodermal
294 lineages and migratory paths of the cells over extended periods encompassing gastrulation
295 and heart tube morphogenesis (~35 hours). Culturing embryos in large volumes of media
296 culture (~1ml) using an open top light sheet microscope was critical to achieve these
297 experiments.

298 Our live-imaging suggests that the cardiac crescent (or first heart field -FHF- and juxta-
299 cardiac field partially overlapping the FHF) [25-28], are predominantly destined to contribute
300 to the LV/AVC. In contrast, the atria arise at different times during gastrulation [1, 2, 7-9].
301 These findings suggest that an early segregation of the ventricular and atrial cells has been
302 conserved during evolution; an early segregation of these progenitor populations was
303 previously shown at single cell resolution in the zebrafish [29-32]. They also align with *in*
304 *vitro* differentiation experiments demonstrating that modulating pathways known to induce
305 mesoderm can generate molecularly distinct mesoderm favouring the generation of
306 ventricular or atrial-like cardiomyocytes respectively [33-37].

307 We found that the early proximal mesoderm harbours multipotent progenitors generating
308 extraembryonic mesoderm, pericardial, endocardial and endothelial-like cells in addition to
309 LV/AVC myocytes. These progenitors became rapidly restricted into unique cardiac fates
310 during migration - prior to the establishment of the cardiac crescent and onset of myocyte

311 differentiation. The observation of short-lived multipotent cardiac progenitors is consistent
312 with clonal analysis results of *Hand1*+ and *Mesp1*+ mesodermal progenitors [1-3].

313 Previous migration analysis noted opposing cell density and motility gradients in the
314 mesoderm [6]. According to this model, cells continually exchange neighbours and disperse
315 widely until their movements gradually diminish, eventually settling in positions and fates as
316 gastrulation concludes. Our live-imaging analysis builds upon these findings, offering a more
317 detailed and prolonged evaluation of the migratory paths of cells in relation to their future
318 fates. The analysis revealed that progenitors contributing to LV/AVC and atrial myocytes
319 remain as separated cell populations throughout migration, establishing two distinct
320 progenitor domains in the heart tube without mixing. During ontogeny, the pericardial and
321 myocardial layers, along with the subjacent plexus of elongated endocardial cells, emerge in
322 close proximity within the cardiac crescent [38]. The migratory trajectories of progeny
323 contributing to these three distinct cardiac fates were more deterministic than previously
324 recognised. Sister cells contributing to the same fate tended to exhibit similar migratory
325 paths. In the future, it will be crucial to discern whether early mesodermal progenitors exhibit
326 similar migratory paths because of similarities in their initial internal state and their ability to
327 interpret environmental cues in a cell-specific manner.

328 Previous studies in zebrafish indicated that G-protein-coupled receptor signalling, a hallmark
329 of chemokine signalling, regulates heart progenitor movements during gastrulation [39-41].
330 Moreover, BMP, Nodal, and FGF morphogen gradients regulate cell migration independently
331 of cell fate [42-46]. Thus, it seems that mesodermal cells respond to morphogen cues with
332 precision, providing determinism to the morphogenetic cell behaviours. Simultaneously, they
333 demonstrate plasticity regarding their final fate [47]. While progenitors are seen giving rise to
334 only one cardiac cell type, they could potentially generate additional cardiac fates when no

335 longer constrain by positional cues. We propose that achieving a delicate balance between
336 determinism and plasticity is essential to ensure robust morphogenesis. This balance enables
337 cells to follow specific developmental pathways while also maintaining the flexibility needed
338 to adapt to changing external cues.

339 Together, our live-imaging analysis of migration and cardiac lineages provide evidence that
340 some regulation of directionality of cell movements and fate allocation may exist early within
341 the mesoderm. The findings have broader implications for our understanding of
342 organogenesis since they address how initial differences between progenitors and signalling
343 cues may ultimately affect the fate and movements of cells.

344 Material and Methods

345 Experimental model and subject details

346 All animal procedures were performed in accordance with the Animal (Scientific Procedures)
347 Act 1986 under the UK Home Office project licenses PP8527846 (Crick) and
348 PP3483414 (UCL) and PIL IA66C8062.
349

350 Mouse strains

351 The $T^{nEGFP\text{-}CreERT2/+}$(MGI:5490031) and $Foxa2^{nEGP\text{-}CreERT2/+}$ (MGI:5490029) lines were obtained from
352 Hiroshi Sasaki. The $R26^{Tomato\ Ai14/\ Tomato\ Ai14}$ ($Gt(ROSA)26Sor^{tm14(CAGtdTomato)Hze}$ (MGI:3809524), were
353 obtained from the Jackson Laboratory. The $(no\ gene)^{Tg(BRE:H2B;Turquoise)Jbri}$ BMP reporter line was
354 generated by the Briscoe laboratory previously [7].

355 Generation of the cTnnT-2a-eGFP line

356 The C -terminal tagging of cardiac troponin cTnnt2 with eGFP was generated in the Genetic
357 Modification Service using CRISPR-Cas9 strategy. This editing was performed by co-
358 transfection of a Cas9-gRNA vector and a donor vector comprising the T2A self-cleaving
359 peptide and eGFP into B6N 6.0 embryonic stem cells using Lipofectamine 2000. The donor
360 vector contained a 786bp insert of T2A-eGFP with 1kb homology arms either side. The guide
361 sequence used was 5'-TTTCATCTATTTCCAACGCC -3'. Two correctly targeted ESC
362 clones were microinjected into blastocysts which were then transfered into the uterus of
363 pseudo pregnant BRAL (C57BL/6 albino) females. Generated chimeras were crossed to
364 BRAL and F0 chimera offspring were initially screened for the proper integration of T2A -
365 eGFP by Sanger sequencing. The F0 were again crossed to BRAL to confirm germline
366 transmission of the mutation and F1 mice were validated by Sanger sequencing.

367 **Immunostaining**

368 Embryos were dissected in 1x Phosphate buffered saline (PBS, Invitrogen), fixed for 4 hours
369 in 4% PFA at room temperature, washed with 1x PBS-0.1% Triton (0.1% PBS-T) and
370 permeabilised in 0.5% PBS-T. Embryos were blocked with 1% donkey serum for 1hr,
371 incubated overnight at 4deg with antibodies diluted in 0.1% PBS-T: mouse anti-cTnnT
372 (1:250, Thermo Fischer Scientific Systems, MS295P0). Embryos were washed in 0.1% PBS-
373 T at room-temperature and incubated overnight at 4deg with secondary antibodies coupled to
374 555 fluorophores (1:200, Molecular Probes). After washing with 0.1% PBS-T, embryos were
375 then incubated overnight at 4deg with DAPI (1:1000). Embryos were washed in 0.1% PBS-T
376 and mounted in vectashield. Confocal images were obtained on an inverted Sp5 confocal
377 microscope with a 20X oil objective (for early E6.5-E7.5 embryos) or a 10X air objective
378 (0.4 NA) (for E12.5 hearts) at a 2048 × 2048 pixels dimension with a z-step of 1 to 5 μm.

379 Embryos were systematically imaged throughout from top to bottom. Images were processed
380 using Fiji software [48].
381
382 **Embryo culture**
383 Embryos were dissected at E6.5 in a solution of DMEM (Dulbecco's Modified Eagle
384 Medium- D5921 Sigma-Aldrich) with 10% FBS (Fetal Bovine Serum- A5256701 Thermo
385 Fisher), 25 mM HEPES-NaOH (pH 7.2), penicillin, and streptomycin. The dissection was
386 done on a stereoscope microscope with a Tokai Hit thermoplate at 37 °C. Dissection was
387 completing within 5 minutes and immediately transfer to media culture to preserve the
388 embryo's developmental potential. Media culture was a mixture of 75% freshly prepared rat
389 serum (filtered through a 0.2-mm filter) and 25% DMEM (containing 1 mg/ml D-glucose and
390 pyruvate, without phenol red and L-glutamine- D5921 Sigma-Aldrich), supplemented with
391 1× glutamax, 100 units/ml penicillin, 100 μg/ml streptomycin, and 11 mM HEPES. The rat
392 serum was prepared according to established protocols [49, 50], stored at –80 °C, heat-
393 inactivated at 56 °C for 30 minutes, and filtered through a 0.22-μm filter before use. All
394 media were equilibrated with a mixture of 5% O2, 5% CO2, and 90% N2, and warmed to
395 37 °C before adding embryos.
396
397 **Multiphoton microscopy**
398 To hold embryos in position during time-lapse acquisition, we made bespoke plastic holders
399 with holes of different diameters (0.3 to 05 mm) to ensure a good fit for the ectoplancental
400 cone similarly to the traps developed by Nonaka and colleagues [51]. Embryos were mounted
401 with their anterior side facing up. To avoid evaporation, the medium was covered with
402 mineral oil (Sigma-Aldrich; M8410). Before starting the time-lapse acquisition, embryos
403 were precultured for at least 2 hours in the microscopy culture set up. For the acquisition, we

404 used the multiphoton Olympus FVMPE-RS equipped with a 5% CO2 incubator and a heating
405 chamber maintaining 37°C. The objective lens used was a HCX APO L 20x/1.00 W dipping
406 objective, which allowed a 2-mm working distance for imaging mouse embryos. A
407 SpectraPhysics MaiTai DeepSee pulsed laser was set at 880 nm and used for one-channel
408 two-photon imaging. Image settings was: output power: 250 mW, pixel dwell time: 7 µs, line
409 averaging: two and image dimension: 610 × 610 µm (1,024 × 1,024 pixels). The z step was 6
410 µm.
411
412 **Light sheet microscopy**
413 For all light sheet acquisitions, we imaged *TnEGFP-CreERT2*/+; *R26 Tomato Ai14*/ *Tomato*
414 *Ai14*, *cTnnT-2a-GFP*+/- embryos. Tamoxifen (T5648 SIGMA) was dissolved in corn oil.
415 Oral gavage was performed (0.02 mg/body weight) at indicated embryonic stages. Embryos
416 were dissected at least 12 hours after. Before the time-lapse acquisition, embryos were
417 precultured for at least 2 hours in the microscopy culture set-up. To hold embryos in position
418 during the acquisition, we embedded part of the ectoplacental cone in Matrigel growth factor
419 reduced phenol red-free (Corning Cat. No 356231) diluted two times with culture medium in
420 a dedicated open-top FEP sample chamber containing an array of four chambers. Typically, 1
421 embryo was mounted per well, totalling 4 per experiment. Pixel size was 2 µm x 0.347 x
422 0.347 (z, x, y). The Viventis LS1 used a single view and dual illumination light sheet.
423 Detection was done using a Nikon 25X NA 1.1 water immersion objective with final 18.7X
424 magnification generating a field of view of 800 x 800 µm. Ilumination with the 488 and 561
425 lasers was sequential. Image acquisition was performed every 2 mins and in stacks totalling
426 500 µm. Exposure times for GFP and tdTomato detection was 50ms and 100ms. Light sheet
427 thickness was 3.3 μm. Embryos were incubated at 37°C in 8% CO2 with humidification
428 throughout.

429

430 **Cell tracking**

431 The original images underwent conversion into HDF5/XML file formats and registration
432 using BigSticher [14], following the methodology outlined in prior work [6]. Subsequently,
433 these processed images were imported into the MaMuT Fiji plugins for manual cell tracking
434 [5]. The MaMut viewer windows allowed visualization of each tracked cell at any brightness,
435 scale, and rotation parameters. Cell identification is initiated at the initial time point, with
436 manual tracking occurring every five-time points, except during mitosis. During mitosis,
437 tracking was performed at every time-point to capture daughter cell separation accurately.
438 The TrackScheme lineage browser was employed to visualize the reconstructed cell lineage
439 tree. Tracked cells were depicted as nodes interconnected by edges, and cell divisions were
440 illustrated as split branches. For subsequent analysis, the tracked cells' spots, tracks, cell
441 division time and GFP intensities were exported in csv format.

442

443 **Threshold analysis**

444 GFP values were normalized based on the highest GFP value within each movie's tracking
445 data. To discern GFP-positive cells from the background, we implemented the following
446 approach: GFP background intensities were measured at regular intervals throughout each
447 movie and linear interpolation was applied between time points to establish a background
448 value for every time-point. The threshold for distinguishing GFP-positive and GFP-negative
449 cells was determined by using a multiple of the mean background. The threshold was set to
450 the lowest multiplier, ensuring that every endocardial cell in each movie were classified as
451 GFP-negative.

452

453 **Lineage analysis**

Each reconstructed lineage tree starts with a mother cell. The mother divides giving rise to the two daughter cells D1 and D2. Then D1 divides giving rise to daughters D11 an D12. D11 divides giving rise to daughters D111 and D112. Lineage trees were generated in R version 4.3.2 using the 'ggtree' version 3.10.0 package [52] with Newick format and imported into R through the 'read.tree' function from the 'ape' package version 5.7.1. The branch lengths of the trees are proportional to the cell cycle length. The trees were coloured using the 'scale_colour_gradient' function in the 'ggtree' package, which imparts a colour gradient based on the normalized GFP intensities of the cells or paintsubtree function in phytools version 2.03 package [53]in R version 4.3.2 (https://www.R-project.org).

Homotypic and Heterotypic Distances Calculation

Trajectories were reconstructed in 3D using matplotlib version 3.7.2 package in Python 3.11.53. We computed Euclidean distances to quantify the spatial relationships among cells, categorizing them into 'homotypic distances' when comparing cells of the same fate and 'heterotypic distances' when comparing cells of different fates. Progenitors' coordinates were sampled before cTnnT-2a-eGFP signal was observed. We only considered branches lasting at least 4 hours into the cell cycle to allow sufficient cell migration. To analyse the evolution of homotypic and heterotypic distances over time, we focused on daughters' coordinates at three distinct time points: T0, T1, and T2. T0: 20 minutes after the mother's initial cell division. T1: last time point before the daughters' subsequent cell division. T2: final time point at which all granddaughter cells exist. If no third generation is present, we only considered branches lasting at least 4 hours into the cell cycle to allow sufficient cell migration.

Midpoint Calculations

477 The midpoints between D1's and D2's progeny were first determined by averaging their
478 coordinates. Progenitors' coordinates were sampled before cTnnT-2a-eGFP signal was
479 observed. Subsequently, a midpoint distance between D1 and D2's progeny's midpoints was
480 calculated.

481 **Dynamic time warping (DTW)**

482 We analyzed migratory trajectories within cardiac lineages by comparing the paths of sister
483 cells from the time immediately following the division of their mother cell to the final time
484 point before the first sister cell division. Trajectory similarity was assessed using the 'dtw-
485 python' (version 1.3.0) Python package, measuring the dynamic time warping distance
486 (DTW) between the cells. We opted for DTW distance over Euclidean distance, as DTW
487 accommodates cells with spatially similar yet temporally nonsynchronous trajectories [52,
488 53]. We applied the 'symmetricP1' step pattern, a slope-constrained step pattern [22, 23]. To
489 determine whether DTW distances between sister cells, whether sharing the same fate or
490 having distinct fates, exhibited significant differences, we performed a permutation test using
491 the 'scipy' Python package (Version 1.11.1) [54]. This involved 100,000 resamplings and the
492 calculation of differences between log mean DTW distances for unipotent and bipotent cells
493 in each permutation. The resulting p-value was computed as the proportion of permuted
494 values greater than or equal to the observed values + 1, divided by the total number of
495 permutations + 1. Our null hypothesis assumed no difference in log mean DTW distances
496 between sister cells generated by unipotent and bipotent progenitors, while the alternative
497 hypothesis suggested a significant difference.

498 ## Figure Legends

499 **Figure 1. Development and Characterisation of the cTnnT-2a-GFP line. (A)** Schematics
500 illustration of a CRISPR-cas9-mediated strategy to insert a 2a-GFP cassette in front of the
501 stop codon into the cTnnT2 gene. **(B-C)** Representative immunofluorescence staining for
502 cTnnT2 in hearts at different stages in cTnnT-2a-GFP mice. Scale bar at E8: 100 µm. Scale
503 bar at E12.5: 200 µm **(D)** Image sequence from time-lapse video of an *TnGPF-CreERT2/+;*
504 *Bre:H2B-Turquoise; cTnnT-2a-GFP* embryo. Scale bar: 100 µm. IF: Inflows, HT: heart tube,
505 OFT: outflow tract, LV: left ventricle, RV: right ventricle, RA: right atria, LA: left atria, YS:
506 Yolk Sac, Ant: Anterior, Post: posterior,

507 **Figure 2**. **Long-term live-imaging from gastrulation to heart tube formation**.
508 **(A)** Schematic of the cell tracking procedure. Tracks carry information on (i) reporter
509 expression, (ii) lineage relationships and (iii) trajectories. **(B)** Image sequences from three
510 time-lapse videos of *TnGPF-CreERT2/+; R26tdtomato+/-; cTnnT-2a-GFP* embryos
511 resulting from the administration of tamoxifen (0.02mg/body weight) at indicated times.
512 LV/AVC: left ventricle and atrio ventricular canal. Scale bar: 100 µm

513 **Figure 3. Independent LV/AVC and Atria progenitors contribute to distinct regions of**
514 **the heart tube. (A)** Reconstruction of mesodermal cell lineages. Cell types are indicated at
515 the endpoints. Lineages are coloured according to their normalised GFP intensities. **(B)** Only
516 the progenitors contributing to at least one cTnnT-2a-GFP+ progenitors are represented. (i)
517 Fate map depicting early (green) and late (magenta) mesoderm contributing to distinct
518 regions of the heart tube (ii) Each colour represents a distinct clone. (iii) cTnnT-2a-GFP+
519 cells are shown in red. **(C)** Fate map showing all the early mesodermal progenitors coloured
520 coded by fate. **(D)** Birth date of progenitors contributing to cTnnT-2a-GFP+ LV/AVC and

521 cTnnT-2a-GFP+ Atria myocytes. The cells already present at the beginning of the movie are
522 highlighted in a grey-dotted box. **(E)** Timepoints at which LV/AVC and atrial progenitors'
523 GFP intensities are above a certain threshold value and defined as GFP-positive cells
524 (Material and Methods) For LV/AVC progenitors, the mean differentiation time is 19.0 hours
525 +/-2.2 and for atrial progenitors it is 30.2 hours +/-2.4; mean +/- SD. **(F)** Time between the
526 first and last progenitor to become cTnnT-2a-GFP+ in every lineage tree contributing to
527 myocytes. Mean time for LV/AVC is 2.5 hours +/-1.7 (SD) and 2.3 hours +/-2.6 -SD), p=
528 0.44. The statistical analysis was done using a Mann-Whitney test. **(G)** Birth date of
529 unipotent progenitors for LV/AVC and atrial myocytes, endocardium and pericardium. The
530 cells already present at the beginning of the movie are highlighted in a grey-dotted box. **(H-**
531 **I)** Image sequences from time-lapse video of *TnGPF-CreERT2/+; R26tdtomato+/-; cTnnT-*
532 *2a-GFP* embryos depicting an LV/AVC (H) and Atrial (I) progenitors. The corresponding
533 lineage tree coloured by the normalised GFP intensity of the track cells are shown in H' and
534 I'. Arrows point to the cells in the lineage tree in H' and I'. Scale bar: 100 µm

535 **Figure 4. Lineage analysis in time-lapse movies demonstrates unipotent and bipotent**
536 **mesodermal progenitors exist. (A-C and E)** Image sequences from time-lapse videos
537 of *TnGPF-CreERT2/+; R26tdtomato+/-; cTnnT-2a-GFP* embryos depicting an unipotent
538 pericardium (A) and an Endocardial and Extra-embryonic mesoderm (B), an endocardial and
539 myocyte (C) and endothelial-like and Extra-embryonic bipotent progenitors (E). The
540 corresponding lineage tree coloured by the normalised GFP intensity of the track cell are
541 shown in A'-C' and E'. Arrows point to the cells represented in the lineage tree in A'-C' and
542 E'. **(D)** Image sequences from time-lapse videos of *TnGPF-CreERT2/+; R26tdtomato+/-;*
543 *cTnnT-2a-GFP* embryos depicting an endocardial progenitor migrating inside the forming
544 heart tube. Scale bar: 100 µm

545 **Figure 5. Cell migration analysis in lineages reveals hidden patterns. (A)** Dispersion
546 analysis over time shows the distances between all daughters and granddaughters in all the
547 cardiac lineages at time points T0, T1, and T2, as explained in the results and material
548 method sections. The average distances at T0 (n=28), T1 (n=28) and T2 (n=136) are 15.2 μm
549 +/- 3.1; 39.08 μm +/- 46.26 and 60.25 μm +/- 67.75, mean +/- SD; T0 vs T1, p=0.027; T1 vs
550 T2, p=0.040. Results were statistically analysed using an uncorrected Dunn's test following a
551 Kruskal-Wallis test (P<0.001). (**B**) Schematic diagram of the hypothesis. If cells migrate
552 randomly, then the unipotent and bipotent progeny will generate equally dispersed daughters
553 by the end of the migration. Alternatively, unipotent progeny will generate less dispersed
554 daughter cells if heterogeneity in migratory trajectories exist. Midpoint distance depicts the
555 Euclidian distance between the D1's daughters' midpoint and the D2's daughters' midpoint.
556 Homotypic and heterotypic distances are between cells of the same or different fate. (**C**)
557 Dispersion analysis comparing homotypic and heterotypic distances between all daughters
558 and granddaughters in all the cardiac lineages at time points T0, T1, and T2. The average
559 homotypic distances at T0 (n=20), T1 (n=20) and T2 (n=105) are 14.45 μm +/- 3.1, 24.67 μm
560 +/-11.69 and 32.90 μm +/- 19.75, mean +/- SD. The average heterotypic distances at T0
561 (n=11), T1 (n=11) and T2 (n=37) are 16.11 μm +/-2.86, 63.40 μm +/- 67.13 and 104.4 μm +/-
562 89.49, mean +/- SD. Results were statistically analysed using an uncorrected Dunn's test
563 following a Kruskal-Wallis test (P<0.001). Timepoint 0: 9 hours and 40 minutes on average
564 +/- 7.4; Timepoint 1: 17 hours and 30 minutes on average +/- 8.4; Timepoint 2: 22 hours and
565 43 minutes on average +/- 6; +/- SD). (**D**) Dispersion analysis comparing homotypic and
566 heterotypic distances between all daughters and granddaughters for all the cardiac lineages.
567 Coordinates were sampled before the onset of cTnnT-2a-GFP expression in the embryos. The
568 average homotypic and heterotypic distances are 34.82 μm +/-20.38 (n=110) and 137.2 μm
569 +/-118.4 (n=70); mean +/- SD. Results were statistically analysed using a Mann-Whitney

570 test. Timepoints on average were 22 hours +/- 5, +/-SD (**E-F**) Homotypic distances in all
571 lineages generating at least one cTnnT-2a-GFP+ LV/AVC (E) or cTnnT-2a-GFP+ atria (F)
572 myocytes. (**G**) Homotypic distances per fate and in lineages developing in only one fate.
573 Coordinates were sampled before the onset of cTnnT-2a-GFP expression in the embryos. The
574 average homotypic distances for LV/AVC, Atria, Pericardium, Endocardium and ExMeso
575 fates were 33.37 µm +/-20.89 (n=90), 27.30 µm +/- 29.40 (n=34), 36.67 µm +/- 15.14 (n=24),
576 41.66 µm +/- 21.31 (n=18) and 79.09 µm +/- 94.06 (n=38), mean +/- SD. Results were
577 statistically analysed using a Kruskal-Wallis and Dunn's multiple comparisons tests. (**H**)
578 Midpoint analysis comparing distances between D1 and D2's daughters' midpoints in cases
579 where D1 and D2 generate the same fate (unipotent) or different fates (bipotent). Analysis
580 was done for all the cardiac lineages. Coordinates were sampled before the onset of cTnnT-
581 2a-GFP expression in the embryos. The average midpoints distances for unipotent and
582 bipotent progenitors were 32.89 µm +/-20.03 (n=20) and 97.35 µm +/-88.49 (n=16), mean +/-
583 SD. (**I**) Dynamic time warping allows quantifying similarities between two migration
584 paths. (**J**) Dynamic time warping score comparing D1 and D2 cell tracks up to their next cell
585 division in cases where D1 and D2 have the same cardiac fate (unipotent) or distinct fates
586 (bipotent). Results were statistically analysed using a Mann- Whitney test. (**K-L**) log DTW
587 score for all lineages generating only cTnnT-2a-GFP+ LV/AVC (K) or cTnnT-2a-GFP+ atria
588 (L) myocytes. (**M**) Average DTW values over time for D1 and D2 daughters generated by
589 unipotent (red) and bipotent (bleu) progenitors. Shaded blue and red represent the standard
590 error. At step 7 (indicated by an orange arrow), the DTW values for daughters of shared and
591 distinct fates are statistically distinct. Results were statistically analysed using a Mann-
592 Whitney test. (**N-S**) Examples of trajectories and corresponding midpoint distance calculation
593 (O'-T') and lineage trees (O''-T''). The red lines in lineage trees indicate the time points at

594 which the cells' coordinates were sampled for the midpoint analysis. The red lines in the
595 trajectory diagram represents the distances between D1 and D2's daughters' midpoints.

596 **Figure 6. Working Model of early cardiac development. (A)** Early proximal mesodermal
597 cells are initially highly plastic (or multi-potent) but rapidly become committed to specific
598 cardiac fates as they initiate migration towards specific embryonic regions in response to
599 environmental cues. LV/AVC and Atrial progenitors are generated from early and late
600 mesoderm, respectively. LV/AVC progenitors differentiate first into myocytes and establish
601 the cardiac crescent. Atria progenitors differentiate later and generate the heart tube's
602 inflows. (**B**) Pair of sisters sharing the same fate have more identical migration paths than
603 sisters with distinct fates. PS: primitive streak. LV/AVC: left ventricle/atrioventricular canal.
604 ExM: Extra-embryonic mesoderm.

605 **Figure 2-supplementary figure 1. Tamoxifen induces tdTomato expression in *TnGPF-*
606 *CreERT2/+; R26tdtomato+/-; cTnnT-2a-GFP* embryos at the correct embryonic stages.**
607 **(A)** Image sequence *TnGPF-CreERT2/+; R26tdtomato+/-; cTnnT-2a-GFP* embryos resulting
608 from the administration of tamoxifen (0.02mg/bw) at E5.5, and culture from E6 to E7 in the
609 absence of tamoxifen. Arrows point to tdTomato-positive cells present in the Extra-
610 embryonic mesoderm. PS: primitive streak. Scale bar: 100 μm

611 **Figure 2-supplementary figure 2. GFP signal Quantification. (A, D and G)**
612 Quantification of the cTnnT-2a-GFP signal in the cardiac crescent and inflows over time. (**B-**
613 **C, E-J, H-F**) We quantified cTnnT-2a-GFP expression by drawing "circles" in the cardiac
614 crescent (B, E and H) and inflows (C, J and F) at different time points. We synchronised the
615 three movies according to their onset of cTnnT-2a-GFP expression in the initial cardiac
616 crescent and subsequent heart tube inflows generated during morphogenesis.

617 **Figure 2-supplementary figure 3. Threshold analysis (A-C)** Green lines represent the
618 threshold set to discern GFP-positive cells from the background**. (D)** Red round circles
619 represent the areas in which the background GFP intensity was measured.

620 **Figure 3-supplementary figure 1. Independent progenitors contribute to the LV/AVC**
621 **and Atria. (A)** Only the progenitors contributing to at least one cTnnT-2a-GFP+ progenitors
622 are represented. In i-iii is movie 2 and in iv-xi is movie 3. (i and iv) Fate map depicting early
623 (green) and late (magenta) mesoderm contributing to distinct regions of the heart tube. (ii and
624 v) Each colour represents a distinct clone. (iii and vi) cTnnT-2a-GFP+ cells are shown in red.
625 Scale bar: 100 µm

626 **Figure 4-supplementary figure 1. Tripotent mesodermal progenitors exist. (A)** Image
627 sequences from time-lapse video of *TnGPF-CreERT2/+; R26tdtomato+/-; cTnnT-2a-*
628 *GFP* embryos depicting a progenitor contributing to three cell types. The corresponding
629 lineage tree coloured by the normalised GFP intensity of the track cells are shown in A'.
630 Arrows point to the cells represented in the lineage tree in A'. Scale bar: 100 µm

631 **Figure 5-supplementary figure 1. Cardiac progenitor trajectories analysis.** (**A-B**)
632 Examples of trajectories and corresponding midpoint distance calculation (A'-A') and lineage
633 trees (A''-B'''). The red lines in lineage trees indicate the time points at which the cells'
634 coordinates were sampled for the midpoint analysis. The red lines in the trajectory diagram
635 represents the distances between D1 and D2 daughters' midpoints. (**C**) Histogram showing
636 the distribution of the permutated tests obtained by calculating the log mean difference
637 between randomly shuffled unipotent and bipotent dynamic time warping (DTW) distances.
638 The data were binned at 30µm intervals. A red dashed line marks the observed log mean
639 difference.

640 **Video 1-3:** Live-imaging from gastrulation to heart tube stage. Embryos are *T*$^{nGPF\text{-}CreERT2/+}$;
641 *R26*$^{tdTomato\text{f}/+}$; cTnnT-2a-GFP. Pregnant mice received tamoxifen at around E6 (Videos 1-2)
642 and E6.5 (Video 3). Images are Maximum projection of 250 sections acquired every 2 µm.
643 Interval between frames: 2 minutes. Related to Fig.2 B.

644 **Video 4:** Example of a myocyte progenitor visualised along the xy and yz axis. From video 2.
645 Scale bar: 50 µm.

646 **Video 5:** Example of an endocardial progenitor visualised along the xy and yz axis. From
647 video 1. Scale bar: 50 µm.

648 **Video 6:** Example of a pericardial progenitor visualised along the xy and yz axis. From video
649 3. Scale bar: 50 µm.

650 ## Acknowledgments

651 We thank Dr Martin Dominguez for their initial help with BigSticher and MaMut. We thank
652 Dr Rosie Marshall and Prof. Andrew Copp for their help with rat serum preparation. We also
653 thank the Light Microscopy facilities and Biological Research Facilities at the Francis Crick
654 Institute and UCL for their help with imaging, image analysis and transgenic colonies. We
655 thank Drs Nancy Stathopoulou and Florencia Cavodeassi for comments on the manuscript.
656 We thank all members of the Ivanovitch and Alexandre labs for help, advice, reagents, and
657 feedback.

658 ## Author Contribution

659 S.A. Conceptualization, Formal analysis, Investigation, Visualization, Writing – review &
660 editing, P.A.E. Methodology, Writing – review & editing, A.C. Methodology, Writing –
661 review & editing, S.V.B. Methodology, J.A.D. Methodology, Supervision, Writing – review

& editing, J.B. Funding acquisition, Supervision, Writing – review & editing, K.I. Funding acquisition, Project Administration, Conceptualization, Formal analysis, Investigation, Visualization, Supervision, Writing – original draft, Writing – review & editing.

Funding

This work was funded by BHF (FS/IBSRF/21/25085) to K.I. S.A. received a 4-year BHF PhD Studentships (FS/4yPhD/F/22/34181). P.A.E. and J.A.D. were supported by the Radiation Research Unit at the Cancer Research UK City of London Centre Award [C7893/A28990]. This work was also supported by the Francis Crick Institute, which receives its core funding from Cancer Research UK, the UK Medical Research Council and Wellcome Trust (all under FC001051) to J.B. Research infrastructure within the Institute of Child Health, UCL is supported by the NIHR Great Ormond Street Hospital Biomedical Research Centre. The views expressed are those of the authors and not necessarily those of the NHS, the NIHR or the Department of Health.

Data Availability

All relevant data are within the paper and its Supporting Information files.

Competing interests

The authors have declared that no competing interests exist.

679 **References**

680 1. Zhang Q, Carlin D, Zhu F, Cattaneo P, Ideker T, Evans SM, et al. Unveiling
681 Complexity and Multipotentiality of Early Heart Fields. Circ Res. 2021;129(4):474-87. Epub
682 20210624. doi: 10.1161/CIRCRESAHA.121.318943. PubMed PMID: 34162224; PubMed
683 Central PMCID: PMCPMC9308985.

684 2. Lescroart F, Chabab S, Lin X, Rulands S, Paulissen C, Rodolosse A, et al. Early
685 lineage restriction in temporally distinct populations of Mesp1 progenitors during mammalian
686 heart development. Nat Cell Biol. 2014;16(9):829-40. Epub 20140824. doi:
687 10.1038/ncb3024. PubMed PMID: 25150979; PubMed Central PMCID: PMCPMC6984965.

688 3. Devine WP, Wythe JD, George M, Koshiba-Takeuchi K, Bruneau BG. Early
689 patterning and specification of cardiac progenitors in gastrulating mesoderm. Elife. 2014;3.
690 Epub 20141008. doi: 10.7554/eLife.03848. PubMed PMID: 25296024; PubMed Central
691 PMCID: PMCPMC4356145.

692 4. Cohen-Gould L, Mikawa T. The fate diversity of mesodermal cells within the heart
693 field during chicken early embryogenesis. Dev Biol. 1996;177(1):265-73. doi:
694 10.1006/dbio.1996.0161. PubMed PMID: 8660893.

695 5. Wolff C, Tinevez JY, Pietzsch T, Stamataki E, Harich B, Guignard L, et al. Multi-
696 view light-sheet imaging and tracking with the MaMuT software reveals the cell lineage of a
697 direct developing arthropod limb. Elife. 2018;7. Epub 20180329. doi: 10.7554/eLife.34410.
698 PubMed PMID: 29595475; PubMed Central PMCID: PMCPMC5929908.

699 6. Dominguez MH, Krup AL, Muncie JM, Bruneau BG. Graded mesoderm assembly
700 governs cell fate and morphogenesis of the early mammalian heart. Cell. 2023;186(3):479-96
701 e23. doi: 10.1016/j.cell.2023.01.001. PubMed PMID: 36736300; PubMed Central PMCID:
702 PMCPMC10091855.

703 7. Ivanovitch K, Soro-Barrio P, Chakravarty P, Jones RA, Bell DM, Mousavy Gharavy
704 SN, et al. Ventricular, atrial, and outflow tract heart progenitors arise from spatially and
705 molecularly distinct regions of the primitive streak. PLoS Biol. 2021;19(5):e3001200. Epub
706 20210517. doi: 10.1371/journal.pbio.3001200. PubMed PMID: 33999917; PubMed Central
707 PMCID: PMCPMC8158918.

708 8. Bardot E, Calderon D, Santoriello F, Han S, Cheung K, Jadhav B, et al. Foxa2
709 identifies a cardiac progenitor population with ventricular differentiation potential. Nat
710 Commun. 2017;8:14428. Epub 20170214. doi: 10.1038/ncomms14428. PubMed PMID:
711 28195173; PubMed Central PMCID: PMCPMC5316866.

712 9. Gonzalez DM, Schrode N, Ebrahim TAM, Broguiere N, Rossi G, Drakhlis L, et al.
713 Dissecting mechanisms of chamber-specific cardiac differentiation and its perturbation
714 following retinoic acid exposure. Development. 2022;149(13). Epub 20220708. doi:
715 10.1242/dev.200557. PubMed PMID: 35686629; PubMed Central PMCID:
716 PMCPMC9340554.

717 10. Saykali B, Mathiah N, Nahaboo W, Racu ML, Hammou L, Defrance M, et al. Distinct
718 mesoderm migration phenotypes in extra-embryonic and embryonic regions of the early
719 mouse embryo. Elife. 2019;8. Epub 20190405. doi: 10.7554/eLife.42434. PubMed PMID:
720 30950395; PubMed Central PMCID: PMCPMC6450669.

721 11. Christiaen L, Davidson B, Kawashima T, Powell W, Nolla H, Vranizan K, et al. The
722 transcription/migration interface in heart precursors of Ciona intestinalis. Science.
723 2008;320(5881):1349-52. doi: 10.1126/science.1158170. PubMed PMID: 18535245.

724 12. Szymczak AL, Workman CJ, Wang Y, Vignali KM, Dilioglou S, Vanin EF, et al.
725 Correction of multi-gene deficiency in vivo using a single 'self-cleaving' 2A peptide-based
726 retroviral vector. Nat Biotechnol. 2004;22(5):589-94. Epub 20040404. doi: 10.1038/nbt957.
727 PubMed PMID: 15064769.

728 13. Ivanovitch K, Temino S, Torres M. Live imaging of heart tube development in mouse
729 reveals alternating phases of cardiac differentiation and morphogenesis. Elife. 2017;6. Epub
730 20171205. doi: 10.7554/eLife.30668. PubMed PMID: 29202929; PubMed Central PMCID:
731 PMCPMC5731822.

732 14. Horl D, Rojas Rusak F, Preusser F, Tillberg P, Randel N, Chhetri RK, et al.
733 BigStitcher: reconstructing high-resolution image datasets of cleared and expanded samples.
734 Nat Methods. 2019;16(9):870-4. Epub 20190805. doi: 10.1038/s41592-019-0501-0. PubMed
735 PMID: 31384047.

736 15. Malin-Mayor C, Hirsch P, Guignard L, McDole K, Wan Y, Lemon WC, et al.
737 Automated reconstruction of whole-embryo cell lineages by learning from sparse
738 annotations. Nat Biotechnol. 2023;41(1):44-9. Epub 20220905. doi: 10.1038/s41587-022-
739 01427-7. PubMed PMID: 36065022; PubMed Central PMCID: PMCPMC7614077.

740 16. Sugawara K, Cevrim C, Averof M. Tracking cell lineages in 3D by incremental deep
741 learning. Elife. 2022;11. Epub 20220106. doi: 10.7554/eLife.69380. PubMed PMID:
742 34989675; PubMed Central PMCID: PMCPMC8741210.

743 17. Moorman A, Webb S, Brown NA, Lamers W, Anderson RH. Development of the
744 heart: (1) formation of the cardiac chambers and arterial trunks. Heart. 2003;89(7):806-14.
745 doi: 10.1136/heart.89.7.806. PubMed PMID: 12807866; PubMed Central PMCID:
746 PMCPMC1767747.

747 18. Wei Y, Mikawa T. Fate diversity of primitive streak cells during heart field formation
748 in ovo. Dev Dyn. 2000;219(4):505-13. doi: 10.1002/1097-0177(2000)9999:9999<::AID-
749 DVDY1076>3.0.CO;2-6. PubMed PMID: 11084650.

750 19. Kelly RG, Brown NA, Buckingham ME. The arterial pole of the mouse heart forms
751 from Fgf10-expressing cells in pharyngeal mesoderm. Dev Cell. 2001;1(3):435-40. doi:
752 10.1016/s1534-5807(01)00040-5. PubMed PMID: 11702954.

753 20. Mjaatvedt CH, Nakaoka T, Moreno-Rodriguez R, Norris RA, Kern MJ, Eisenberg
754 CA, et al. The outflow tract of the heart is recruited from a novel heart-forming field. Dev
755 Biol. 2001;238(1):97-109. doi: 10.1006/dbio.2001.0409. PubMed PMID: 11783996.

21. Waldo KL, Kumiski DH, Wallis KT, Stadt HA, Hutson MR, Platt DH, et al. Conotruncal myocardium arises from a secondary heart field. Development. 2001;128(16):3179-88. doi: 10.1242/dev.128.16.3179. PubMed PMID: 11688566.

22. Zaffran S, Kelly RG, Meilhac SM, Buckingham ME, Brown NA. Right ventricular myocardium derives from the anterior heart field. Circ Res. 2004;95(3):261-8. Epub 20040624. doi: 10.1161/01.RES.0000136815.73623.BE. PubMed PMID: 15217909.

23. Sakoe H, Chiba S. Dynamic-Programming Algorithm Optimization for Spoken Word Recognition. Ieee T Acoust Speech. 1978;26(1):43-9. doi: Doi 10.1109/Tassp.1978.1163055. PubMed PMID: WOS:A1978EN09300006.

24. Shokoohi-Yekta M, Hu B, Jin H, Wang J, Keogh E. Generalizing DTW to the multi-dimensional case requires an adaptive approach. Data Min Knowl Discov. 2017;31(1):1-31. Epub 20160215. doi: 10.1007/s10618-016-0455-0. PubMed PMID: 29104448; PubMed Central PMCID: PMCPMC5668684.

25. Liang X, Wang G, Lin L, Lowe J, Zhang Q, Bu L, et al. HCN4 dynamically marks the first heart field and conduction system precursors. Circ Res. 2013;113(4):399-407. Epub 20130606. doi: 10.1161/CIRCRESAHA.113.301588. PubMed PMID: 23743334; PubMed Central PMCID: PMCPMC4017870.

26. Spater D, Abramczuk MK, Buac K, Zangi L, Stachel MW, Clarke J, et al. A HCN4+ cardiomyogenic progenitor derived from the first heart field and human pluripotent stem cells. Nat Cell Biol. 2013;15(9):1098-106. Epub 20130825. doi: 10.1038/ncb2824. PubMed PMID: 23974038.

27. Tyser RCV, Ibarra-Soria X, McDole K, Arcot Jayaram S, Godwin J, van den Brand TAH, et al. Characterization of a common progenitor pool of the epicardium and myocardium. Science. 2021;371(6533). Epub 20210107. doi: 10.1126/science.abb2986. PubMed PMID: 33414188.

28. Watanabe Y, Wang Y, Tanaka Y, Iwase A, Kawamura T, Saga Y, et al. Hey2 enhancer activity defines unipotent progenitors for left ventricular cardiomyocytes in juxta-cardiac field of early mouse embryo. Proc Natl Acad Sci U S A. 2023;120(37):e2307658120. Epub 20230905. doi: 10.1073/pnas.2307658120. PubMed PMID: 37669370; PubMed Central PMCID: PMCPMC10500178.

29. Stainier DY, Lee RK, Fishman MC. Cardiovascular development in the zebrafish. I. Myocardial fate map and heart tube formation. Development. 1993;119(1):31-40. doi: 10.1242/dev.119.1.31. PubMed PMID: 8275863.

30. Yutzey KE, Bader D. Diversification of cardiomyogenic cell lineages during early heart development. Circ Res. 1995;77(2):216-9. doi: 10.1161/01.res.77.2.216. PubMed PMID: 7614708.

31. Keegan BR, Meyer D, Yelon D. Organization of cardiac chamber progenitors in the zebrafish blastula. Development. 2004;131(13):3081-91. Epub 20040602. doi: 10.1242/dev.01185. PubMed PMID: 15175246.

795 32. Garcia-Martinez V, Schoenwolf GC. Primitive-streak origin of the cardiovascular
796 system in avian embryos. Dev Biol. 1993;159(2):706-19. doi: 10.1006/dbio.1993.1276.
797 PubMed PMID: 8405690.

798 33. Dark N, Cosson MV, Tsansizi LI, Owen TJ, Ferraro E, Francis AJ, et al. Generation
799 of left ventricle-like cardiomyocytes with improved structural, functional, and metabolic
800 maturity from human pluripotent stem cells. Cell Rep Methods. 2023;3(4):100456. Epub
801 20230424. doi: 10.1016/j.crmeth.2023.100456. PubMed PMID: 37159667; PubMed Central
802 PMCID: PMCPMC10163040.

803 34. Mendjan S, Mascetti VL, Ortmann D, Ortiz M, Karjosukarso DW, Ng Y, et al.
804 NANOG and CDX2 pattern distinct subtypes of human mesoderm during exit from
805 pluripotency. Cell Stem Cell. 2014;15(3):310-25. Epub 20140718. doi:
806 10.1016/j.stem.2014.06.006. PubMed PMID: 25042702.

807 35. Lee JH, Protze SI, Laksman Z, Backx PH, Keller GM. Human Pluripotent Stem Cell-
808 Derived Atrial and Ventricular Cardiomyocytes Develop from Distinct Mesoderm
809 Populations. Cell Stem Cell. 2017;21(2):179-94 e4. doi: 10.1016/j.stem.2017.07.003.
810 PubMed PMID: 28777944.

811 36. Schmidt C, Deyett A, Ilmer T, Haendeler S, Torres Caballero A, Novatchkova M, et
812 al. Multi-chamber cardioids unravel human heart development and cardiac defects. Cell.
813 2023. Epub 20231116. doi: 10.1016/j.cell.2023.10.030. PubMed PMID: 38029745.

814 37. Yang D, Gomez-Garcia J, Funakoshi S, Tran T, Fernandes I, Bader GD, et al.
815 Modeling human multi-lineage heart field development with pluripotent stem cells. Cell Stem
816 Cell. 2022;29(9):1382-401 e8. doi: 10.1016/j.stem.2022.08.007. PubMed PMID: 36055193.

817 38. DeRuiter MC, Poelmann RE, VanderPlas-de Vries I, Mentink MM, Gittenberger-de
818 Groot AC. The development of the myocardium and endocardium in mouse embryos. Fusion
819 of two heart tubes? Anat Embryol (Berl). 1992;185(5):461-73. doi: 10.1007/BF00174084.
820 PubMed PMID: 1567022.

821 39. Zeng XX, Wilm TP, Sepich DS, Solnica-Krezel L. Apelin and its receptor control
822 heart field formation during zebrafish gastrulation. Dev Cell. 2007;12(3):391-402. doi:
823 10.1016/j.devcel.2007.01.011. PubMed PMID: 17336905.

824 40. Scott IC, Masri B, D'Amico LA, Jin SW, Jungblut B, Wehman AM, et al. The g
825 protein-coupled receptor agtrl1b regulates early development of myocardial progenitors. Dev
826 Cell. 2007;12(3):403-13. doi: 10.1016/j.devcel.2007.01.012. PubMed PMID: 17336906.

827 41. Kupperman E, An S, Osborne N, Waldron S, Stainier DY. A sphingosine-1-phosphate
828 receptor regulates cell migration during vertebrate heart development. Nature.
829 2000;406(6792):192-5. doi: 10.1038/35018092. PubMed PMID: 10910360.

830 42. Ciruna B, Rossant J. FGF signaling regulates mesoderm cell fate specification and
831 morphogenetic movement at the primitive streak. Dev Cell. 2001;1(1):37-49. doi:
832 10.1016/s1534-5807(01)00017-x. PubMed PMID: 11703922.

833 43. Nutt SL, Dingwell KS, Holt CE, Amaya E. Xenopus Sprouty2 inhibits FGF-mediated
834 gastrulation movements but does not affect mesoderm induction and patterning. Genes Dev.
835 2001;15(9):1152-66. doi: 10.1101/gad.191301. PubMed PMID: 11331610; PubMed Central
836 PMCID: PMCPMC312687.

837 44. Yang X, Dormann D, Munsterberg AE, Weijer CJ. Cell movement patterns during
838 gastrulation in the chick are controlled by positive and negative chemotaxis mediated by
839 FGF4 and FGF8. Dev Cell. 2002;3(3):425-37. doi: 10.1016/s1534-5807(02)00256-3.
840 PubMed PMID: 12361604.

841 45. von der Hardt S, Bakkers J, Inbal A, Carvalho L, Solnica-Krezel L, Heisenberg CP, et
842 al. The Bmp gradient of the zebrafish gastrula guides migrating lateral cells by regulating
843 cell-cell adhesion. Curr Biol. 2007;17(6):475-87. Epub 20070301. doi:
844 10.1016/j.cub.2007.02.013. PubMed PMID: 17331724.

845 46. Guo Q, Li JY. Distinct functions of the major Fgf8 spliceform, Fgf8b, before and
846 during mouse gastrulation. Development. 2007;134(12):2251-60. Epub 20070516. doi:
847 10.1242/dev.004929. PubMed PMID: 17507393; PubMed Central PMCID:
848 PMCPMC2518685.

849 47. Tam PP, Parameswaran M, Kinder SJ, Weinberger RP. The allocation of epiblast cells
850 to the embryonic heart and other mesodermal lineages: the role of ingression and tissue
851 movement during gastrulation. Development. 1997;124(9):1631-42. doi:
852 10.1242/dev.124.9.1631. PubMed PMID: 9165112.

853 48. Schindelin J, Arganda-Carreras I, Frise E, Kaynig V, Longair M, Pietzsch T, et al.
854 Fiji: an open-source platform for biological-image analysis. Nat Methods. 2012;9(7):676-82.
855 Epub 20120628. doi: 10.1038/nmeth.2019. PubMed PMID: 22743772; PubMed Central
856 PMCID: PMCPMC3855844.

857 49. Cockroft DL, Brook FA, Copp AJ. Inositol deficiency increases the susceptibility to
858 neural tube defects of genetically predisposed (curly tail) mouse embryos in vitro.
859 Teratology. 1992;45(2):223-32. doi: 10.1002/tera.1420450216. PubMed PMID: 1615432.

860 50. Takahashi M, Makino S, Kikkawa T, Osumi N. Preparation of rat serum suitable for
861 mammalian whole embryo culture. J Vis Exp. 2014;(90):e51969. Epub 20140803. doi:
862 10.3791/51969. PubMed PMID: 25145996; PubMed Central PMCID: PMCPMC4672955.

863 51. Ichikawa T, Nakazato K, Keller PJ, Kajiura-Kobayashi H, Stelzer EH, Mochizuki A,
864 et al. Live imaging and quantitative analysis of gastrulation in mouse embryos using light-
865 sheet microscopy and 3D tracking tools. Nat Protoc. 2014;9(3):575-85. Epub 20140213. doi:
866 10.1038/nprot.2014.035. PubMed PMID: 24525751.

867 52. Yu G. Using ggtree to Visualize Data on Tree-Like Structures. Curr Protoc
868 Bioinformatics. 2020;69(1):e96. doi: 10.1002/cpbi.96. PubMed PMID: 32162851.

869 53. Revell LJ. phytools: an R package for phylogenetic comparative biology (and other
870 things). Methods Ecol Evol. 2012;3(2):217-23. doi: 10.1111/j.2041-210X.2011.00169.x.
871 PubMed PMID: WOS:000302538500001.

54. Virtanen P, Gommers R, Oliphant TE, Haberland M, Reddy T, Cournapeau D, et al. SciPy 1.0: fundamental algorithms for scientific computing in Python. Nature Methods. 2020;17(3):261-72. doi: 10.1038/s41592-019-0686-2. PubMed PMID: WOS:000510821500001.

Figure1

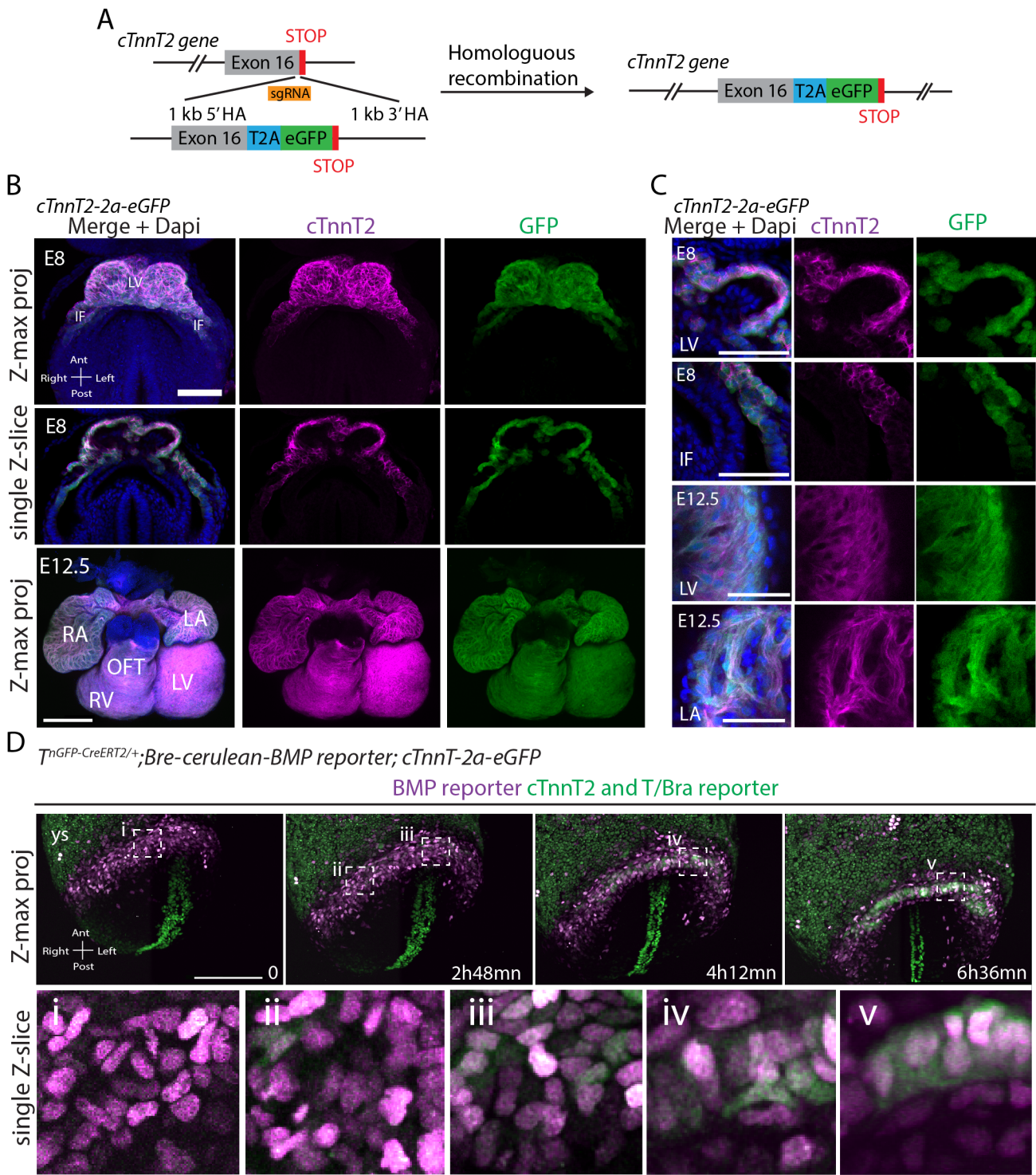
A
cTnnT2 gene
STOP
Exon 16
sgRNA
1 kb 5'HA
1 kb 3'HA
Exon 16 T2A eGFP
STOP
Homologuous recombination
cTnnT2 gene
Exon 16 T2A eGFP
STOP
B
cTnnT2-2a-eGFP
Merge + Dapi
cTnnT2
GFP
Z-max proj
single Z-slice
Z-max proj
E8
LV
IF
IF
Ant
Right
Left
Post
E8
E12.5
RA
LA
OFT
LV
RV
C
cTnnT2-2a-eGFP
Merge + Dapi
cTnnT2
GFP
E8
LV
E8
IF
E12.5
LV
E12.5
LA
D
TnGFP-CreERT2/+;Bre-cerulean-BMP reporter; cTnnT-2a-eGFP
BMP reporter cTnnT2 and T/Bra reporter
Z-max proj
single Z-slice
ys
i
ii
iii
iv
v
Ant
Right
Left
Post
0
2h48mn
4h12mn
6h36mn

Figure2

A

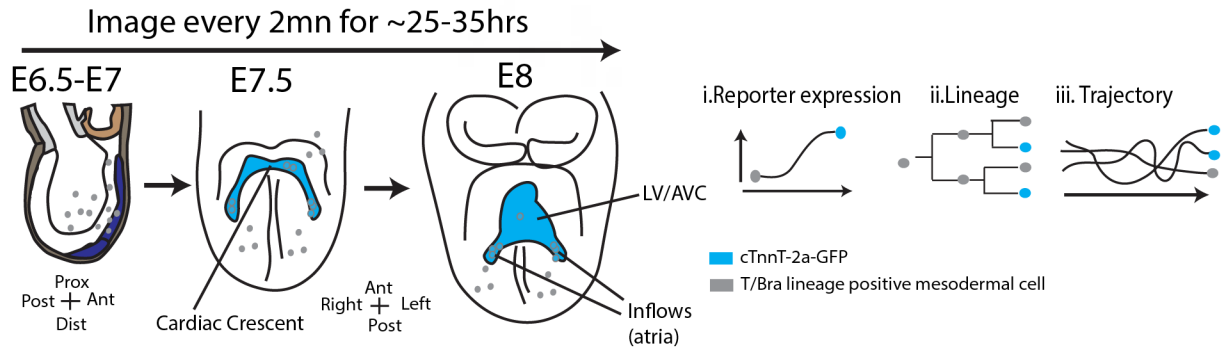

B

$T^{nGFP\text{-}CreERT2/+}$;$R26^{tdtomato/+}$; *cTnnT-2a-eGFP*

T/Bra expression reporter (PS and notochord) T/Bra lineage (mesoderm) cTnnT reporter (cardiomyocytes)

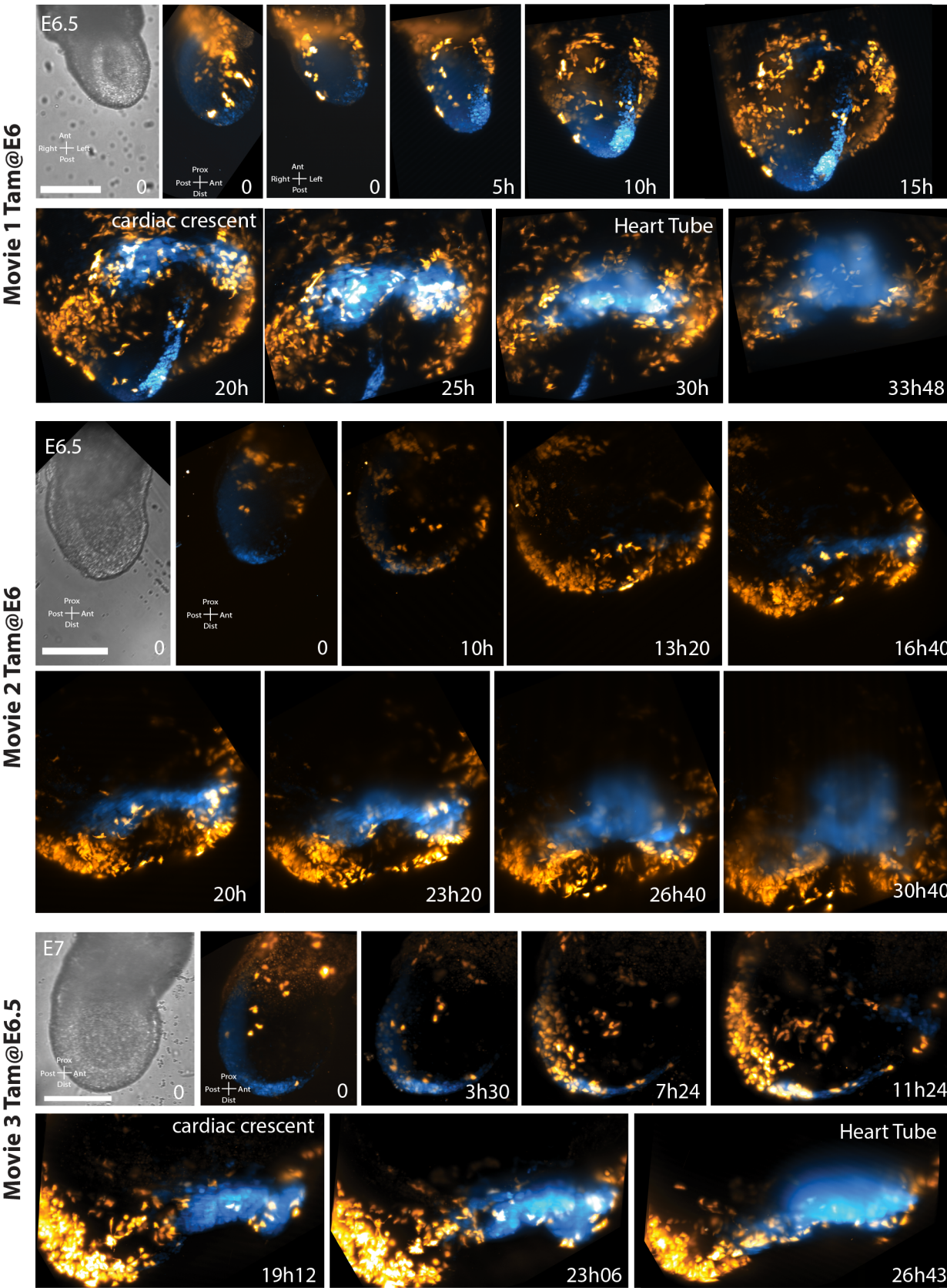

Figure3

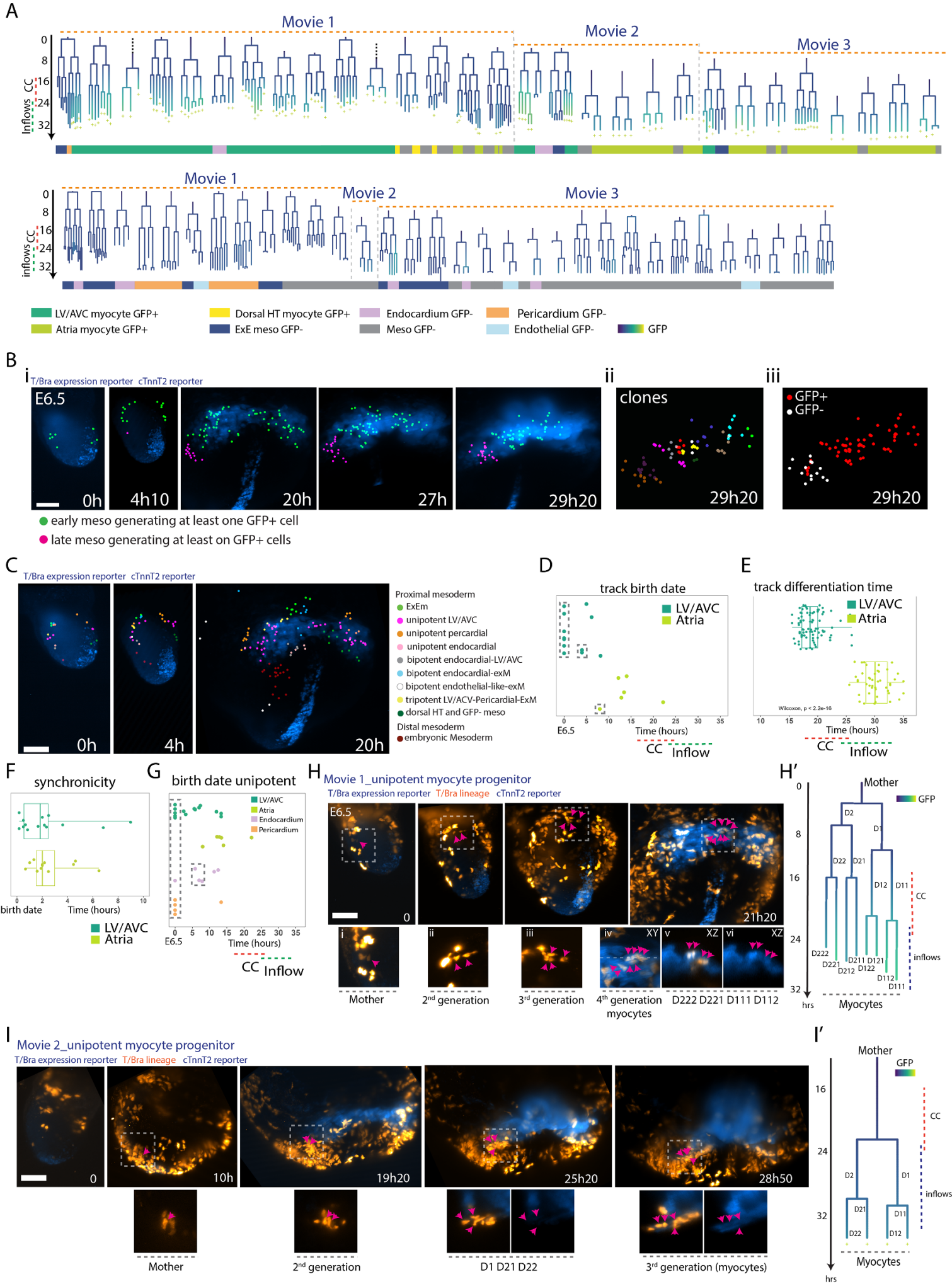
A
Movie 1
Movie 2
Movie 3
Inflows
CC
LV/AVC myocyte GFP+
Atria myocyte GFP+
Dorsal HT myocyte GFP+
ExE meso GFP-
Endocardium GFP-
Meso GFP-
Pericardium GFP-
Endothelial GFP-
GFP
B
i
T/Bra expression reporter cTnnT2 reporter
E6.5
0h
4h10
20h
27h
29h20
ii
clones
29h20
iii
GFP+
GFP-
29h20
early meso generating at least one GFP+ cell
late meso generating at least on GFP+ cells
C
T/Bra expression reporter cTnnT2 reporter
0h
4h
20h
Proximal mesoderm
ExEm
unipotent LV/AVC
unipotent percardial
unipotent endocardial
bipotent endocardial-LV/AVC
bipotent endocardial-exM
bipotent endothelial-like-exM
tripotent LV/ACV-Pericardial-ExM
dorsal HT and GFP- meso
Distal mesoderm
embryonic Mesoderm
D
track birth date
LV/AVC
Atria
E6.5
Time (hours)
CC
Inflow
E
track differentiation time
LV/AVC
Atria
Wilcoxon, p < 2.2e-16
Time (hours)
CC
Inflow
F
synchronicity
birth date
Time (hours)
LV/AVC
Atria
G
birth date unipotent
LV/AVC
Atria
Endocardium
Pericardium
E6.5
Time (hours)
CC
Inflow
H
Movie 1_unipotent myocyte progenitor
T/Bra expression reporter T/Bra lineage cTnnT2 reporter
E6.5
21h20
Mother
2nd generation
3rd generation
4th generation myocytes
D222 D221 D111 D112
H'
Mother
GFP
CC
inflows
hrs
Myocytes
I
Movie 2_unipotent myocyte progenitor
T/Bra expression reporter T/Bra lineage cTnnT2 reporter
10h
19h20
25h20
28h50
Mother
2nd generation
D1 D21 D22
3rd generation (myocytes)
I'
Mother
GFP
CC
inflows
hrs
Myocytes

Figure 4

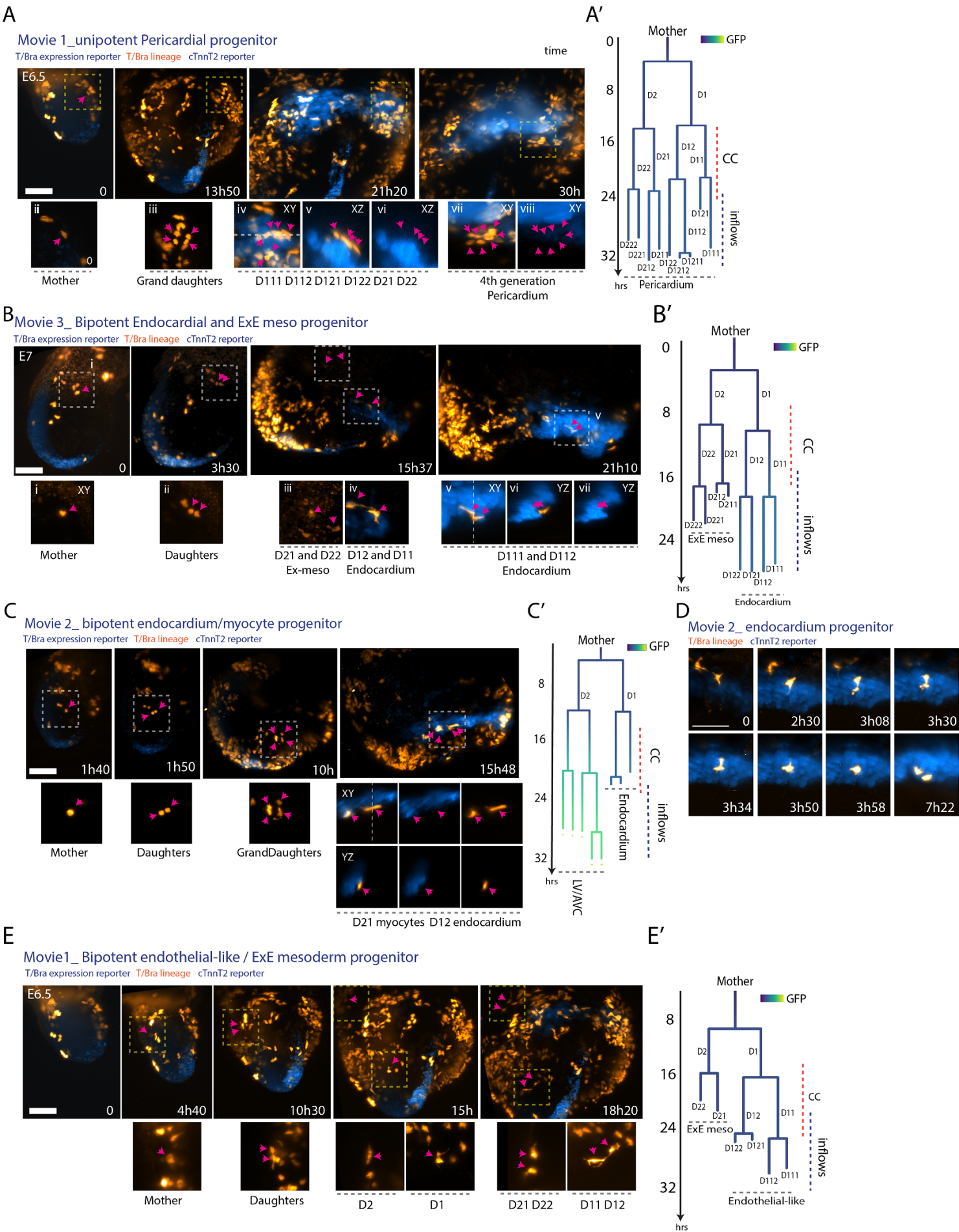
A
Movie 1_unipotent Pericardial progenitor
T/Bra expression reporter T/Bra lineage cTnnT2 reporter
time
E6.5
0
13h50
21h20
30h
Mother
Grand daughters
D111 D112 D121 D122 D21 D22
4th generation Pericardium
A′
Mother
GFP
CC
inflows
hrs
Pericardium
B
Movie 3_ Bipotent Endocardial and ExE meso progenitor
T/Bra expression reporter T/Bra lineage cTnnT2 reporter
E7
3h30
15h37
21h10
Mother
Daughters
D21 and D22 Ex-meso
D12 and D11 Endocardium
D111 and D112 Endocardium
B′
ExE meso
Endocardium
C
Movie 2_ bipotent endocardium/myocyte progenitor
T/Bra expression reporter T/Bra lineage cTnnT2 reporter
1h40
1h50
10h
15h48
Mother
Daughters
GrandDaughters
D21 myocytes D12 endocardium
C′
Endocardium
LV/AVC
D
Movie 2_ endocardium progenitor
T/Bra lineage cTnnT2 reporter
2h30
3h08
3h30
3h34
3h50
3h58
7h22
E
Movie1_ Bipotent endothelial-like / ExE mesoderm progenitor
T/Bra expression reporter T/Bra lineage cTnnT2 reporter
E6.5
4h40
10h30
15h
18h20
Mother
Daughters
D2
D1
D21 D22
D11 D12
E′
ExE meso
Endothelial-like

Figure5

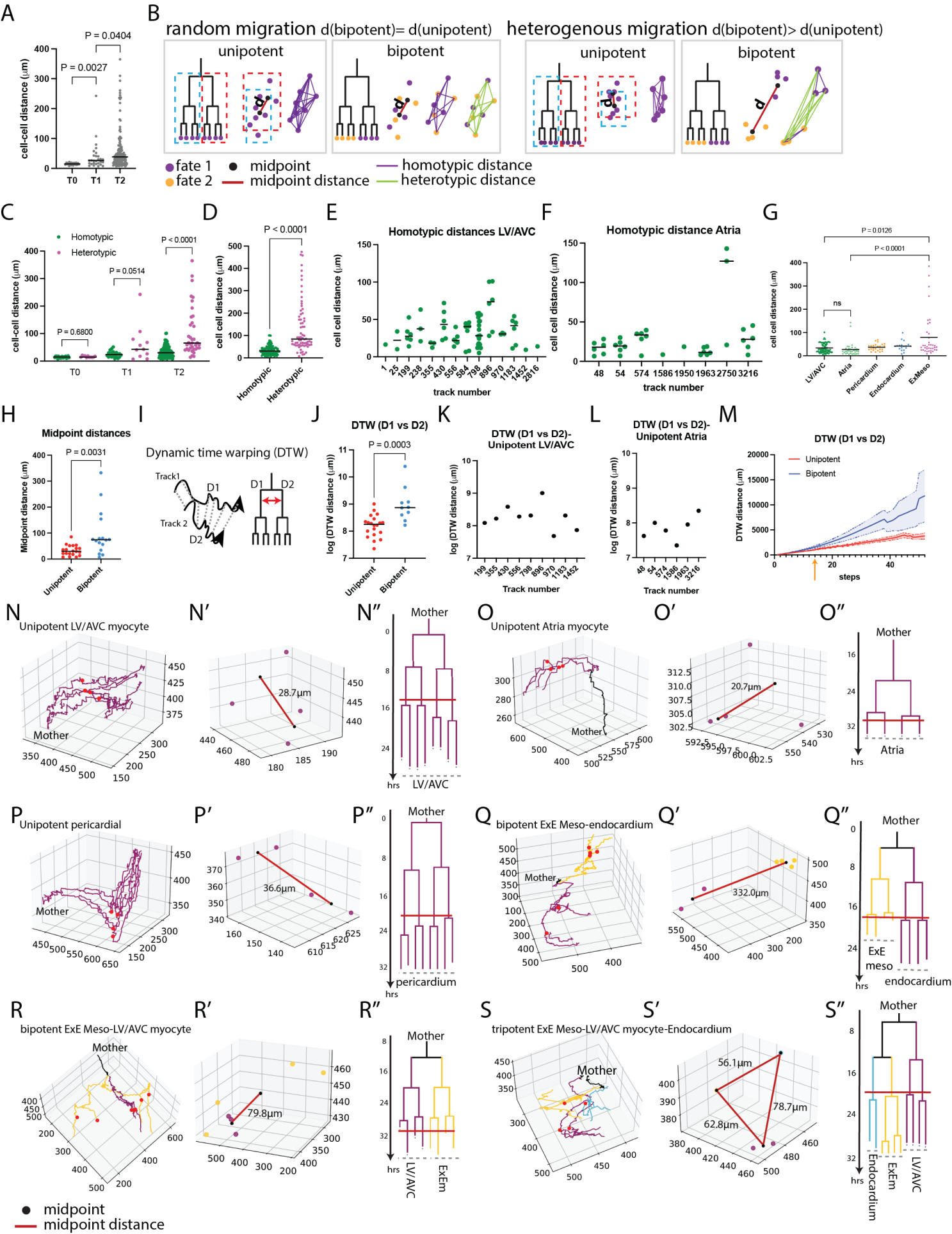
A
P = 0.0404
P = 0.0027
cell-cell distance (µm)
T0
T1
T2
B
random migration d(bipotent)= d(unipotent)
heterogenous migration d(bipotent)> d(unipotent)
unipotent
bipotent
fate 1
fate 2
midpoint
midpoint distance
homotypic distance
heterotypic distance
C
Homotypic
Heterotypic
P = 0.6800
P = 0.0514
P < 0.0001
D
P < 0.0001
Homotypic
Heterotypic
E
Homotypic distances LV/AVC
track number
F
Homotypic distance Atria
track number
G
P = 0.0126
P < 0.0001
ns
LV/AVC
Atria
Pericardium
Endocardium
ExMeso
H
Midpoint distances
P = 0.0031
Midpoint distance (µm)
Unipotent
Bipotent
I
Dynamic time warping (DTW)
Track1
Track 2
D1
D2
J
DTW (D1 vs D2)
P = 0.0003
log (DTW distance (µm))
K
DTW (D1 vs D2)-
Unipotent LV/AVC
Track number
L
DTW (D1 vs D2)-
Unipotent Atria
Track number
M
DTW (D1 vs D2)
Unipotent
Bipotent
DTW distance (µm)
steps
N
Unipotent LV/AVC myocyte
Mother
N′
28.7µm
N″
Mother
hrs
LV/AVC
O
Unipotent Atria myocyte
Mother
O′
20.7µm
O″
Mother
hrs
Atria
P
Unipotent pericardial
Mother
P′
36.6µm
P″
Mother
hrs
pericardium
Q
bipotent ExE Meso-endocardium
Mother
Q′
332.0µm
Q″
Mother
ExE
meso
endocardium
hrs
R
bipotent ExE Meso-LV/AVC myocyte
Mother
R′
79.8µm
R″
Mother
hrs
LV/AVC
ExEm
S
tripotent ExE Meso-LV/AVC myocyte-Endocardium
Mother
S′
56.1µm
78.7µm
62.8µm
S″
Mother
hrs
Endocardium
ExEm
LV/AVC
midpoint
midpoint distance

Figure6

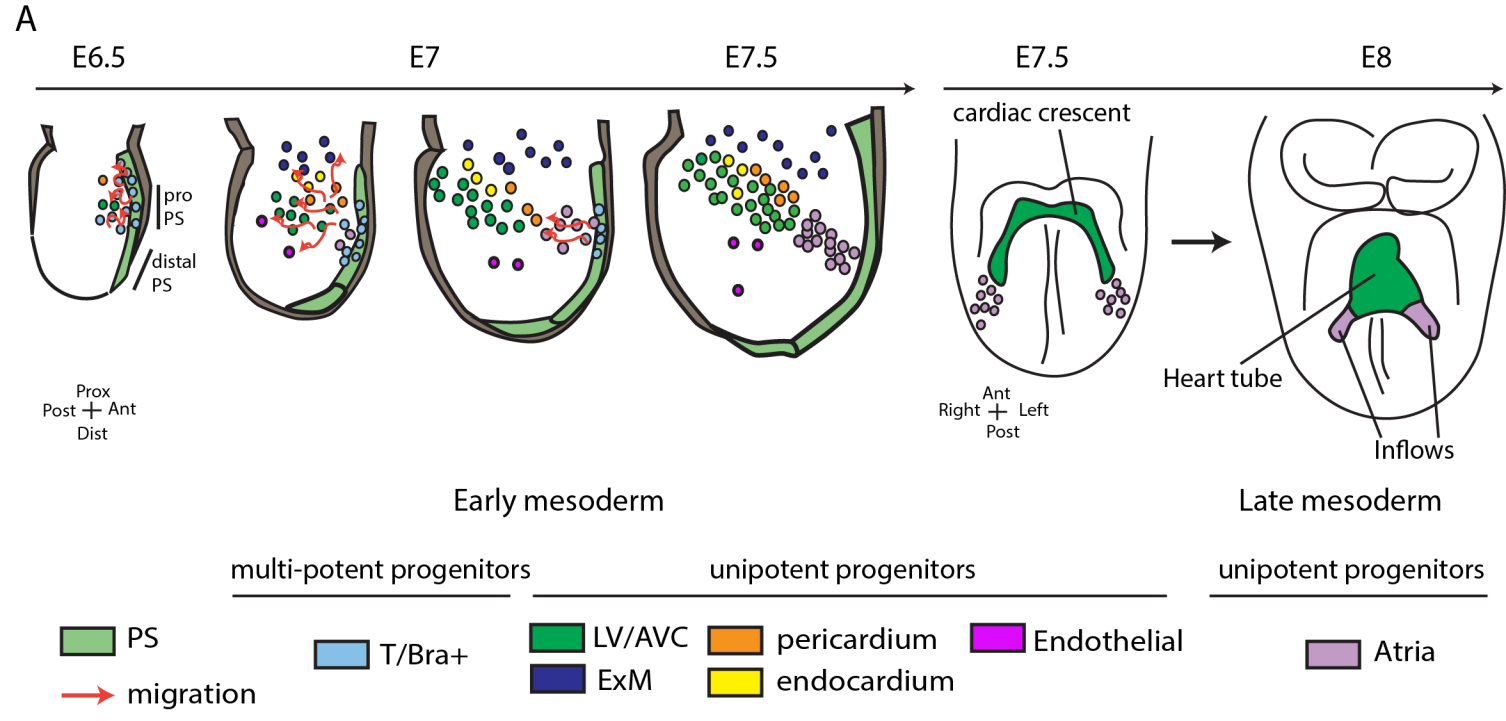
A
E6.5
E7
E7.5
E7.5
E8
pro PS
distal PS
Prox
Post
Ant
Dist
cardiac crescent
Ant
Right
Left
Post
Heart tube
Inflows
Early mesoderm
Late mesoderm
multi-potent progenitors
unipotent progenitors
unipotent progenitors
PS
migration
T/Bra+
LV/AVC
ExM
pericardium
endocardium
Endothelial
Atria

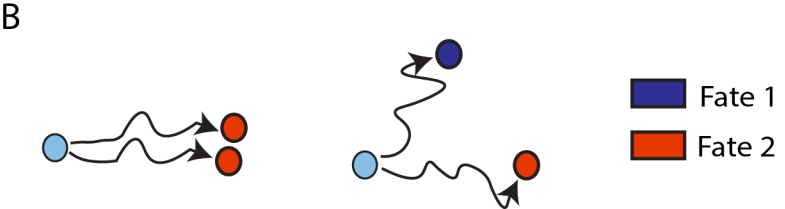
B
Fate 1
Fate 2

Figure2_supplementary figure 1

A

T^nGFP-CreERT2/+;R26^tdtomato/+; cTnnT-2a-eGFP

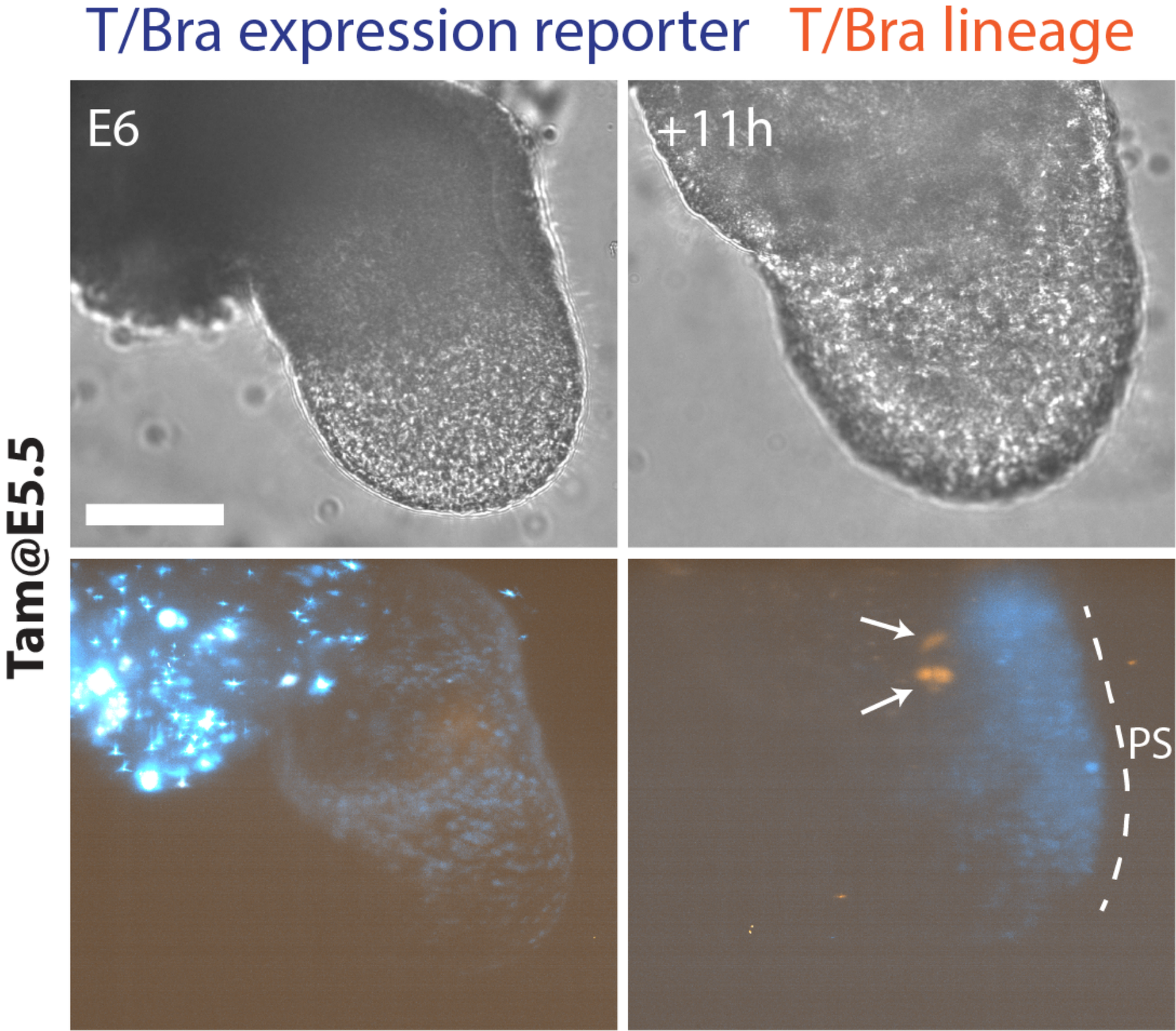

Figure2_supplementary figure 2

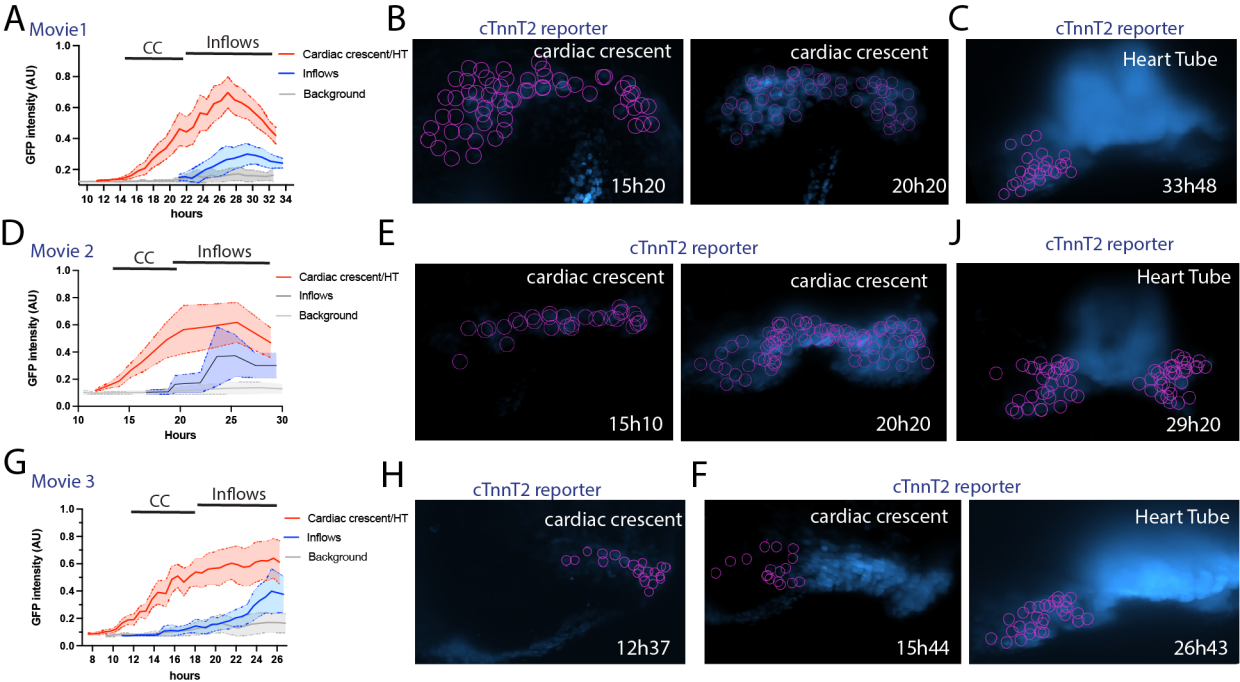

Figure2_supplementary figure 3

A

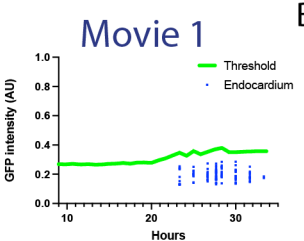

B

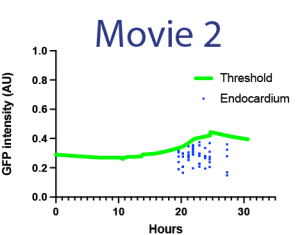

C

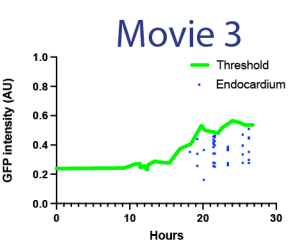

D

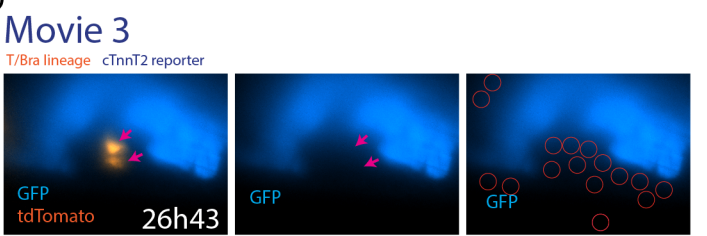

Figure3_supplementary figure 1

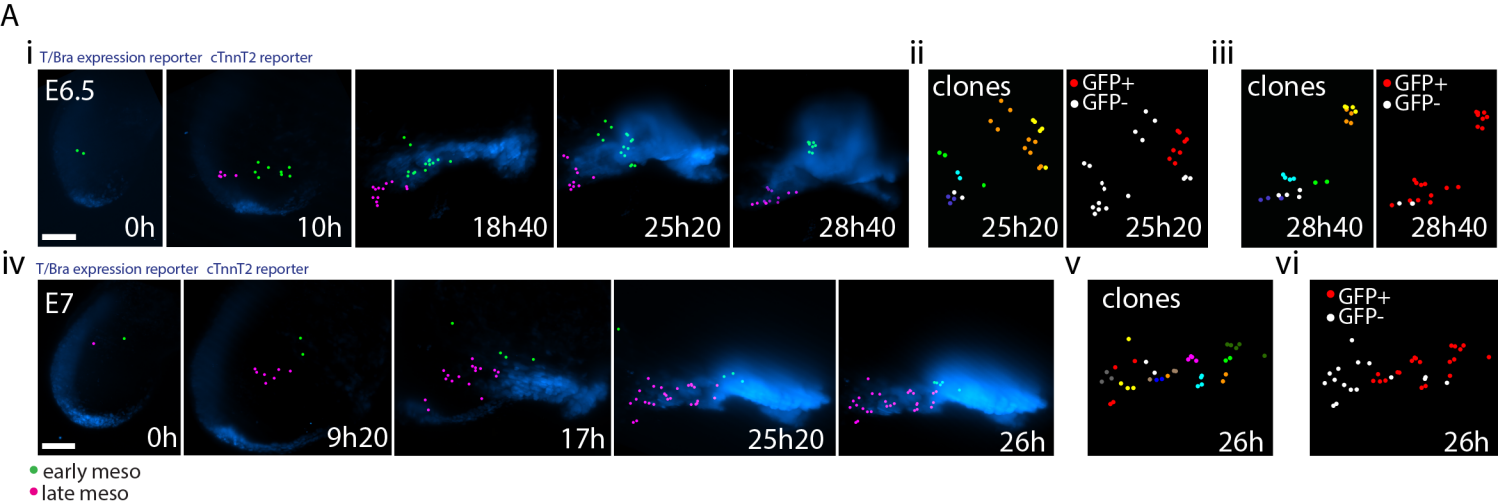

Figure4_supplementary figure 1

A

Movie 3_ tripotent exMeso/endocardium/myocyte progenitor

T/Bra expression reporter T/Bra lineage cTnnT2 reporter

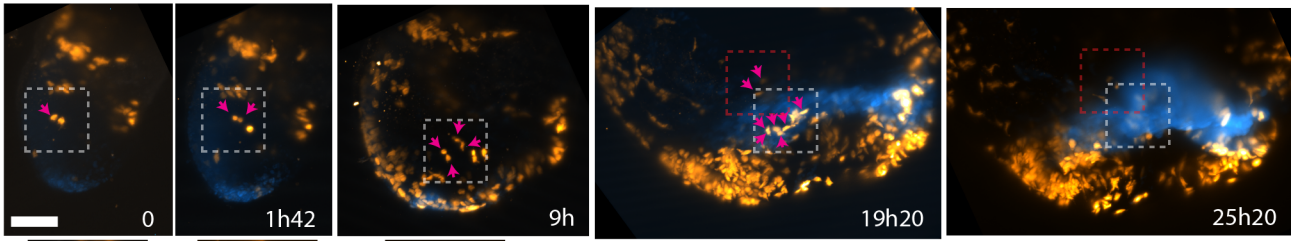

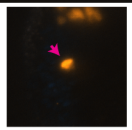

Mother

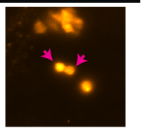

1st generation

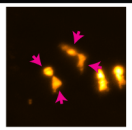

2nd generation

B

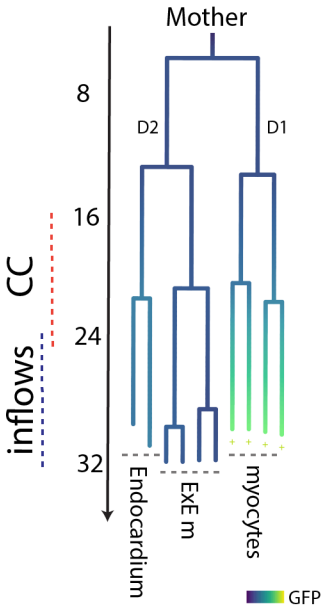

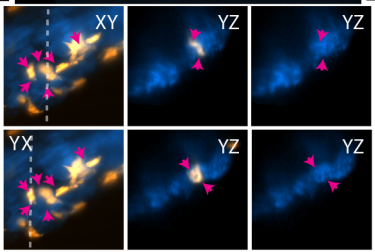

D111 D112 D121 D122 (myocytes)

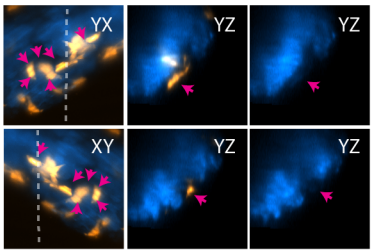

D222 D221 (endocardium)

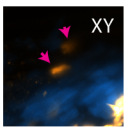

D211 D212
ExMeso

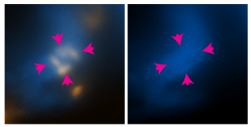

D111 D121 D122 D12
(myocytes)

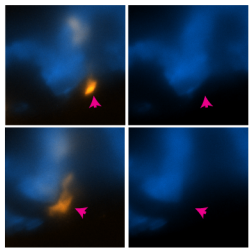

D222 D221 (endocardium)

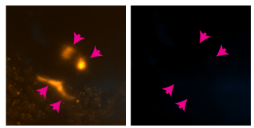

D2111 D2112 D2121 D2122
(ExMeso)

3rd generation

Figure5_supplementary figure 1

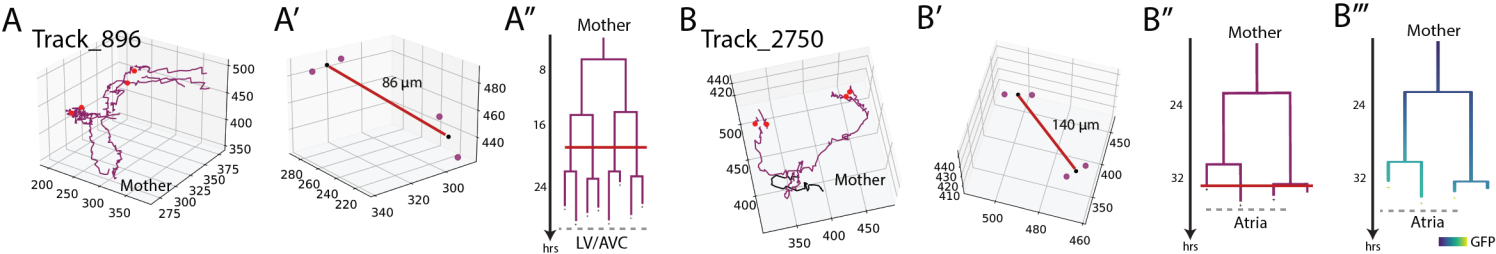
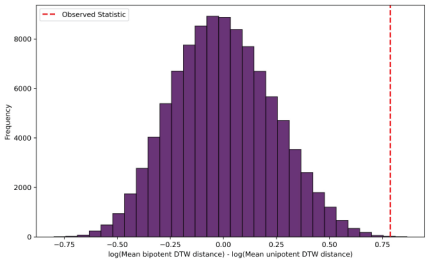
C